



1 Synoptic Ozone, Cloud Reflectivity, and Erythemal Irradiance from Sunrise to Sunset for the Whole Earth  
2 as viewed by the DSCOVR spacecraft from Lagrange-1

3 Jay Herman<sup>1</sup>, Liang Huang<sup>2</sup>, Richard McPeters<sup>3</sup>, Jerry Ziemke<sup>3</sup>, Alexander Cede<sup>4</sup>, Karin Blank<sup>3</sup>

4 Abstract

5 The EPIC instrument onboard the DSCOVR spacecraft, located near the Earth-Sun gravitational plus  
6 centrifugal force balance point, Lagrange-1, measures Earth reflected radiances in 10 wavelength  
7 channels ranging from 317.5 nm to 779.5 nm. Of these channels, four are in the UV range 317.5, 325,  
8 340, and 388 nm, which are used to retrieve O<sub>3</sub>, 388 nm scene reflectivity (LER Lambert Equivalent  
9 Reflectivity), SO<sub>2</sub>, and aerosol properties. These quantities are derived synoptically for the entire sunlit  
10 globe from sunrise to sunset every 68 minutes or 110 minutes for summer or winter at the receiving  
11 antenna in Wallops Island, Virginia, respectively. Depending on solar zenith angle, either 317.5 or 325  
12 nm channels are combined with 340 and 388 nm to derive ozone amounts. As part of the ozone  
13 algorithm, the 388 nm channel is used to derive LER. The retrieved ozone amounts and LER are  
14 combined to derive the erythemal irradiance for the sunlit Earth's surface at a resolution of 18 x 18 km<sup>2</sup>  
15 near the center of the Earth's disk using a computationally efficient approximation to a radiative transfer  
16 calculation of irradiance. Corrections are made for altitude above sea level and for the reduced  
17 transmission by clouds based on retrieved LER.

18

19

20

21 <sup>1</sup>University of Maryland Baltimore County, Maryland

22 <sup>2</sup>Science Systems and Applications, Lanham, Maryland

23 <sup>3</sup>NASA Goddard Space Flight Center, Greenbelt, Maryland

24 <sup>4</sup>SciGlob Instruments and Services, Maryland

25

26



27 DSCOVR/EPIC Synoptic Ozone, Cloud Reflectivity, and Erythral Irradiance From Sunrise to Sunset for  
28 the Whole Earth as viewed from an Earth-Sun Lagrange-1 Orbit

## 29 1.0 Introduction

30 The DSCOVR (Deep Space Climate Observatory) spacecraft was successfully launched on 11  
31 February 2015 to an orbit near the Earth-Sun gravitational plus centrifugal force balance point,  
32 Lagrange-1 (L-1),  $1.5 \times 10^6$  km from the Earth. The earth pointing instruments on the DSCOVR spacecraft  
33 placed in orbit about the L-1 point will simultaneously observe the sun illuminated earth's disk from  
34 sunrise to sunset. An illustration of the orbit is given in the Appendix (see <https://epic.gsfc.nasa.gov> for  
35 details). DSCOVR started to transmit Earth data after it achieved a quasi-stable orbit in mid-June 2015.  
36 The DSCOVR mission at L-1 is optimum for early warning solar flare observations (magnetic field,  
37 electron, and proton fluxes) from instruments contained on the sunward side of DSCOVR, and contains  
38 two Earth-viewing instruments allowing continuous observation of the sunlit face of the Earth. The EPIC  
39 (Earth Polychromatic Imaging Camera) instrument onboard DSCOVR images the Earth in ten narrow  
40 band wavelength channels (up to 2048 x 2048 pixels), producing both color images of the Earth and  
41 science data products such as ozone, SO<sub>2</sub>, aerosol amounts, cloud reflectivity, UV surface irradiance,  
42 cloud and aerosol heights, and vegetation indices. This paper discusses the UV science products O<sub>3</sub>,  
43 cloud reflectivity, and UV surface irradiance, methods of retrieval, and EPIC's UV in-flight calibration.

## 44 1.1 EPIC Instrument

45 The EPIC instrument consists of a 30-cm aperture 283.642 cm focal length Cassegrain telescope  
46 containing a multi-element field-lens group focusing light onto a UV sensitive 2048 x 2048 hafnium  
47 coated CCD detector with 12 bit readout electronics. Images are made through ten narrow-band filters,  
48 four in the ultraviolet, four in the visible, and two in the near infrared. The 10 filter transmission  
49 functions are shown in Fig. 1. Observations are made as light passes sequentially through each of ten  
50 narrow-band filters mounted in two moveable filter wheels and through an exposure control 3-slot  
51 rotating shutter. The exposure times for each wavelength were adjusted in-flight to achieve an  
52 approximately 80 % CCD electron well fill in the brightest scenes, which were observed during the first  
53 week of operation, to avoid saturation and leaking from one pixel to another (blooming). Earth exposure  
54 times range from about 654 milliseconds at 317.5 nm to 22 milliseconds at 551 nm, which have not  
55 changed during the current life of the mission. Another set of exposure times was determined for  
56 viewing the full moon as seen from the Earth (Table 1). The CCD has a well depth of approximately  
57  $8.5 \times 10^4$  electrons (a maximum signal to noise ratio SNR of 290:1) before a small dark current correction  
58 that is a function of its in-flight operating temperature of -20°C. The 12-bit readout means that there  
59 are  $2^{11}$  (2048) readout steps or counts (42 electrons/count). The counts divided by the exposure time  
60 (counts/second) are converted to radiances or albedos using in-flight scene matching calibration from  
61 low earth orbit satellites (see Sect. 1.2 and Table 2). The maximum SNR applies to the brightest of  
62 scenes over high clouds or fresh snow over ice. Cloud-free and snow-free scenes have much lower SNR,  
63 which affects the visible channels more than the UV channels because of the lower scene contrasts with  
64 clouds caused by enhanced UV Rayleigh scattering. There are occasional bright flashes caused by ice



65 crystals in high clouds that saturate a few pixels (see Fig. 2 and Marshak et al., 2017) in the equatorial  
66 and mid-latitude regions.

67 The filters of interest for calculating ozone amounts, aerosol index, and cloud reflectivity are  
68 centered on 317.5, 325, 340, and 388 nm in the wavelength band with full widths at half maximum  
69 (FWHMs) 1.0, 1.0, 2.7, and 2.6 nm, respectively. For the UV channels, 2 x 2 individual pixels are  
70 averaged onboard the spacecraft to yield an effective 1024 x 1024 pixel image corresponding to an 18 x  
71 18 km<sup>2</sup> resolution at the observed center of the Earth's sunlit disk. The effective spatial resolution  
72 decreases as the secant of the angle between EPIC's sub-earth point and the normal to the earth's  
73 surface. Only the 443 nm channel is retrieved at full resolution to help with resolving cloud cover and  
74 obtaining improved color images. The sampling resolution of a single pixel is about 8 x 8 km<sup>2</sup> (about 1  
75 arcsecond), but including the effect of the optical point-spread function, the effective 443 nm channel  
76 resolution is about 10 km. The effective resolution at 443 nm has been verified by looking at clear  
77 scenes over the Nile River in Egypt and, occasionally, the cloud-free Amazon River in Brazil.

78  
79 EPIC data has been obtained since June 15, 2015 at a rate of one set of 10 wavelengths every 68  
80 minutes during Northern Hemisphere (NH) summer and one set every 110 minutes in the winter. The  
81 difference between summer and winter rates is caused by the reduced number of hours in the winter  
82 when the antenna (located at Wallops Island, Virginia) is in view of the spacecraft, and limitations from  
83 the spacecraft memory technology from the late 1990s.

84  
85 Each of the 10-wavelength measurements is obtained at a slightly different times. The first filter  
86 in the sequence is 443 nm, which takes about 2 minutes to complete a measurement (28 ms exposure  
87 time (Table 1) plus CCD readout and onboard processing time that includes 12-bit jpeg compression of a  
88 2048 x 2048 pixel image). The remaining 9 filter measurements take a total of about 5 minutes  
89 (exposure times plus CCD readout into memory) and then another 13 minutes to process the data for  
90 the 9 filters (this includes 12-bit jpeg compression of 1024 x 1024 images that have been averaged  
91 onboard in groups of 2x2 pixels before compression). Adjacent pairs of wavelengths are measured at 30  
92 second intervals before the onboard processing is started. This means the individual channel images are  
93 not co-located at the pixel level because of earth rotation (15.03<sup>o</sup> per hour or about 1670 km per hour  
94 at the equator), the slow rotation of the spacecraft, 0.082<sup>o</sup> per hour, and a small amount of spacecraft  
95 jitter). Each pixel views about 1 arc second or 2.78x10<sup>-4</sup> degrees. Data from an onboard star-tracker and  
96 feedback from the earth's image on the CCD keep the images approximately centered on the CCD. The  
97 lack of native channel-to-channel colocation requires an elaborate spherical geometry geolocation  
98 analysis to adjust the data to a common latitude x longitude grid with an accuracy of 1/4 of a pixel.

99 A description of the EPIC instrument, its orbit, and some of the data products can be obtained  
100 from [http://avdc.gsfc.nasa.gov/pub/DSCOVER/Web\\_EPIC/](http://avdc.gsfc.nasa.gov/pub/DSCOVER/Web_EPIC/) and from <http://epic.gsfc.nasa.gov/>. The EPIC  
101 raw counts/second and science data (Version 2 used in this paper) are archived at  
102 [https://eosweb.larc.nasa.gov/project/dscovr/dscovr\\_table](https://eosweb.larc.nasa.gov/project/dscovr/dscovr_table) in HDF5 format.

103



104 This paper presents examples of the ozone and scene reflectivity retrievals that are used to  
 105 obtain unique estimates of erythemal UV irradiance (or UV Index, UVI) as a function of latitude,  
 106 longitude, local solar time (LST), and altitude above sea level (ASL). Since this is the first paper on EPIC  
 107 retrieved ozone, Sect. 1 contains a brief description of the calibration of the four UV channels and the  
 108 ozone retrieval algorithm. Sect. 2 shows examples of natural color images, Sect. 3 gives an example of  
 109 retrieved ozone and the corresponding 388 nm Lambert Equivalent Reflectivity (LER, Herman et al.,  
 110 2009), Sect. 4 presents a validation of EPIC retrieved ozone compared to ozone from ground-based and  
 111 satellite data, Sect. 5 shows details of the latitudinal and longitudinal synoptic variability of ozone, and  
 112 Sect. 6 presents new results showing the sunrise to sunset variability of UV erythemal radiation reaching  
 113 the Earth's surface including the reduction by clouds from sunrise to sunset.

114 The data and images of the changing synoptic cloud cover from sunrise to sunset are unique to  
 115 the EPIC satellite instrument. Neither geostationary nor low earth orbiting satellites can produce these  
 116 data or images. Geostationary satellites could produce something similar, but to date, none have the UV  
 117 channels for ozone and LER, and geostationary satellites are limited to a range of approximately  $\pm 60^\circ$   
 118 latitude and  $\pm 60^\circ$  longitude. While low earth orbiting satellite data can be combined to produce a global  
 119 representation of ozone and cloud cover, all the ozone and cloud cover are for a fixed local time (e.g.,  
 120 13:30 hours for OMI) and is not representative of the atmosphere at other times of the day.

## 121 1.2 Calibration

122 Before the raw EPIC data (counts per second) can be used, a number of pre-processing steps  
 123 must be accomplished. The major steps are 1) measuring and subtracting the dark current signal, 2)  
 124 "flat-fielding" the CCD so that the sensitivity differences between all four million pixels are determined  
 125 and corrected, 3) correcting for stray-light effects to account for light that should be going to a particular  
 126 pixel, but instead is scattered to different pixels, and 4) determining the radiometric calibration for each  
 127 wavelength channel in terms of EPIC counts/second to be converted to earth normalized radiances or  
 128 reflectances (backscattered at approximately  $172^\circ$ ). The earth upwelling normalized radiance  $I_M$  ( $W/(m^2$   
 129  $nm\ sr)$ ) at the top of the atmosphere (TOA) is defined in terms of the albedo  $A_M$  given by Eq. 1,

$$A_M = \frac{I_M}{S_M/D_E^2} \quad (sr^{-1}) \quad (1)$$

130 for wavelength bands  $M=1$  to 4,  $S_M$  is the incident solar irradiance ( $W/(m^2\ nm)$ ) weighted with the filter  
 131 function for band  $M$  at 1 AU and  $D_E$  is the sun-earth distance in AU (astronomical units). Since EPIC does  
 132 not measure solar irradiance, we use a high resolution solar irradiance spectrum,  $S(\lambda)$  (Dobber et al.,  
 133 2008), as a reference solar spectrum. The reference spectrum is weighted with EPIC's filter transmission  
 134 functions  $T_M(\lambda)$  (Fig. 1) to obtain each EPIC channel's weighted solar irradiance  $S_M$  at solar-earth  
 135 distance at 1 astronomical unit (Eqs. 1 and 2).

$$S_M = \int_{\lambda_1}^{\lambda_2} T_M(\lambda) S(\lambda) d\lambda / \int_{\lambda_1}^{\lambda_2} T_M(\lambda) d\lambda \quad (Wm^{-2}nm^{-1}) \quad (2)$$

136



137 In-flight radiometric calibration is accomplished by comparison with albedo values measured by  
 138 current well-calibrated LEO (low-earth orbiting; e.g., Aura/OMI, Ozone Monitoring Instrument, and  
 139 Suomi-NPP/OMPS, National Polar-orbiting Partnership/Ozone Mapping and Profiler Suite) satellite  
 140 instruments observing scenes that match in time and observing angles with those from EPIC. For albedo  
 141 measurements, OMPS has a calibration accuracy of 2 %, while its wavelength dependence (precision) in  
 142 the calibration is estimated to be better than 1 % (Jaross et al., 2014). The OMPS Nadir Mapper on  
 143 Suomi-NPP has a 50 x 50 km<sup>2</sup> footprint in its normal operating mode with 36 cross-track views (±55°  
 144 satellite view angle or strip of about ±12° equatorial longitude). It has a spectral resolution of 1 nm,  
 145 which is close to EPIC's 317.5 nm and 325 nm channels FWHM, but narrower than EPIC's 340 nm and  
 146 388 nm channels. To perform in-flight calibration, OMPS' albedo spectra were either interpolated (for  
 147 317.5 and 325 nm channels) or convolved (at 340 and 388 nm) with each EPIC filter transmission  
 148 function  $T_M$  (Fig. 1). Because the albedo spectra  $A_M(\lambda)$  (Eq. 1) cancels the solar irradiance  $S_M$  Fraunhofer  
 149 line structure, the interpolation and convolution of  $A_M(\lambda)$  has better accuracy than directly using the  
 150 radiance spectra  $I_M(\lambda)$ . OMI on Aura has 13 x 24 km<sup>2</sup> spatial resolution and about ±56° cross-track views  
 151 (a strip of ± 1300 km or ± 13° equatorial longitude) with a spectral resolution of 0.42 nm. To match  
 152 measurements with DSCOVR, OMI's albedo spectra were convolved with EPIC's  $T_M(\lambda)$ . Then, the results  
 153 in every two adjacent cross-track views and four consecutive along-track scans are combined to form 50  
 154 x 50 km<sup>2</sup> footprints for comparison with EPIC measured counts/second obtained from 7 x 7 EPIC pixels.

155 EPIC raw counts/second inside each coincident footprint are preprocessed by the steps stated in  
 156 a previous paragraph. Then, the counts/second average and variance in each coincident footprint are  
 157 computed to obtain the EPIC albedo calibration coefficients  $K_M$  (Eq. 3). Misalignment between EPIC and  
 158 OMPS or OMI footprints can result large scene noise unless uniform scenes are selected and less  
 159 uniform scenes discarded. This is achieved by weighting each coincident data point with the reciprocal  
 160 of the percent EPIC counts/second variance inside the coincident footprint. All of the coincident points  
 161 between LEO satellites and EPIC observations occur within ±40° of the earth's equator. Selected LEO  
 162 footprints have viewing angles nearly identical to EPIC's (within 1° in backscatter angle and 2° degrees in  
 163 solar zenith angle). EPIC's backscatter angle varies with latitude and longitude by less than 0.25°, since  
 164 the angular size of the earth varies from 0.45° to 0.53° to 0.45° every 6 months depending on the  
 165 location of DSCOVR in its orbit (an irregular Lissajous orbit about L-1 that is tilted relative to the ecliptic  
 166 plane and perturbed by the Earth's moon). The orbit varies from 4° to 15° away from the Earth-Sun line.  
 167 These small differences in observing geometry are corrected in the atmospheric radiative transfer model  
 168 calculations  $\alpha(\lambda)$  (Eq. 4), resulting in corrections less than 2 %. EPIC albedo calibration coefficients are  
 169 derived from Eqs. 3 and 4.

$$K_M = \frac{A_M(OMPS)\{\alpha_M(EPIC)/\alpha_M(OMPS)\}}{C_M(EPIC)D_E^2} \quad (3)$$

$$\alpha_M = \int \alpha(\lambda)S(\lambda)T_M(\lambda) d\lambda / \int S(\lambda)T_M(\lambda) d\lambda \quad (4)$$

170

171 where



172  $M$  is the EPIC channel number,  $M=1,2,3,4$   
 173  $A_M(\text{OMPS})$  = OMPS albedo measurement in the EPIC channel- $M$  wavelength band  
 174  $\alpha_M(\text{EPIC})$  and  $\alpha_M(\text{OMPS})$  are computed albedo values for EPIC and OMPS coincident geometry,  
 175  $C_M(\text{EPIC})$  is the average count rate over the pixels matching OMPS,  
 176  $D_E$  is the sun-earth distance in AU.  
 177  $\alpha(\lambda)$  is the computed high resolution normalized radiance spectrum,  
 178  $S(\lambda)$  is the referenced high resolution solar irradiance spectrum,  
 179  $T_M(\lambda)$  is the EPIC filter transmission profile or the OMPS slit function.

180  
 181 All of the coincidence points with LEO satellite instruments were measured using the area of  
 182 the EPIC CCD within 600 pixels of its center. There are about 15000 coincidence data points accumulated  
 183 by the end of 2016. Because of the large number of data points, statistical averaging errors are small.  
 184 An atmospheric radiative transfer model, RTM, takes total column ozone and surface reflectivity from  
 185 LEO retrievals to obtain both  $\alpha_M(\text{EPIC})$  and  $\alpha_M(\text{LEO})$ . Although uncertainties in the RTM can propagate  
 186 into the computed albedos, the resulting uncertainties in  $\alpha_M(\text{EPIC})$  and  $\alpha_M(\text{LEO})$  are approximately  
 187 identical, and approximately cancel in Eq. 3. The resulting EPIC albedo calibration uncertainty is mostly  
 188 inherited from the OMPS albedo calibration uncertainty, which has an accuracy of 2 % and a precision of  
 189 1 % in relative (wavelength dependent) values. For the UV channels, the calibration factors  $K_M$  are not  
 190 constants, but are slowly increasing functions of time (on average 0.016 per year; see  $K_M(t)$  in Fig. 2),  
 191 which is normalized to one on 1 January 2016). Table 2 shows the reference values of  $K_M$  multiplied by  
 192  $\pi$ .

193 Using Tables 1, 2, and Fig. 2, EPIC albedo measurements are derived with

$$194 \quad A_M(\text{EPIC}) = K_M C_M(\text{EPIC}) D_E^2 \quad (1-5)$$

195  
 196  
 197 Note that the factor  $D_E^2$  for solar irradiance at 1 AU is contained in the albedo calibration  
 198 coefficient  $K_M$ . Since solar activity changes (e.g., 27.5 day cycle) are negligible for EPIC UV channel  
 199 wavelengths, daily solar irradiance changes are only adjusted with the sun-earth distance  $D_E$ . Users of  
 200 EPIC data may also be interested in radiance measurements. The radiance calibration coefficients can  
 201 be derived with Eq. 6,

$$202 \quad E_M = K_M S_M \quad (6)$$

203  
 204  
 205 and the radiance measurements can be obtained with Eq. 7.

$$206 \quad I_M(\text{EPIC}) = E_M C_M(\text{EPIC}) \quad (7)$$

207  
 208  
 209 The uncertainty in the radiance calibration can increase significantly due to errors in estimating  
 210 the absolute solar irradiance. Uncertainty in estimated  $S_M$  for EPIC UV channels in Table 1 is about 3 %.


 211 **1.3 Ozone Algorithm**

212

 213 Once the albedo calibration factors are applied to EPIC's measured counts/second, the  
 214 calculated albedos can be combined to retrieve total column ozone (TCO), Lambert Equivalent  
 215 Reflectivity (LER), and aerosol index (AI). The TOA directional albedo calculation uses the TOMRAD  
 216 radiative transfer calculation code, which has a spherical geometry correction for large solar zenith  
 217 angles (SZA) and satellite looking angles (SLA) (Caudill et al., 1997). The calculation uses the same  
 218 climatological ozone profiles used in OMI retrievals, altitude weighted average effective ozone  
 219 temperatures, ground reflectivities, terrain height, and climatological cloud heights. Spectrally resolved  
 220 O<sub>3</sub> absorption cross sections are from Brion et al., (1993, 1998); Daumont et al., (1992); and Malicet et  
 221 al., (1995). The resulting spectra are convolved with the EPIC filter transmission functions (Fig. 1) and  
 222 with the reference solar irradiance spectra (see Eq. 4).

223

 224 The resulting computed  $\alpha_M$  (Eq. 4) are compiled into a finely stepped look-up table as functions  
 225 of ozone profiles and solar-view angles. EPIC ozone retrieval uses the 388 nm channel for computing  
 226 the surface reflectivity with a formula similar (except for choice of wavelengths) to that used in cloud  
 227 reflectivity studies (Herman et al., 2009). Then, the retrieval is based on two ozone absorption channels,  
 228 317.5 nm and 340 nm for low optical depth conditions, or 325 nm and 340 nm for high optical depth  
 229 conditions, together with the 388 nm measurement to form triplet equations. The ozone retrieval  
 230 algorithm assumes a linear wavelength dependence in the surface reflectivity (Eq. 8),

$$R_\lambda = R_{\lambda_0} + b(\lambda - \lambda_0) \quad (8)$$

231

 232 where  $\lambda_0$  is given wavelength 388 nm. The total column ozone (TCO) is given by Eq. 9,

$$\Omega = \Omega_0 + \frac{\Delta N_{\lambda_1} \frac{\partial N_{\lambda_2}}{\partial R} (\lambda_2 - \lambda_0) - \Delta N_{\lambda_2} \frac{\partial N_{\lambda_1}}{\partial R} (\lambda_1 - \lambda_0)}{\frac{\partial N_{\lambda_1}}{\partial \Omega} \frac{\partial N_{\lambda_2}}{\partial R} (\lambda_2 - \lambda_0) - \frac{\partial N_{\lambda_2}}{\partial \Omega} \frac{\partial N_{\lambda_1}}{\partial R} (\lambda_1 - \lambda_0)} \quad (9)$$

233 where

234  $\Omega_0$  is an initial climatology estimate of TCO or TCO from previous step in the iteration,235  $\lambda_1$  and  $\lambda_2$  are the selected ozone absorption wavelengths,236  $N_\lambda$  is the N-value defined as logarithm of the albedo values by Eq. 10,

237

$$N_\lambda = -100 \log_{10}\{I_\lambda / (S_\lambda / D^2)\} \quad (10)$$

238

239 and

240  $\Delta N_\lambda$  is the N-value residue (difference between the measured N-value and the computed N-value),



241  $\frac{\partial N_{\lambda_x}}{\partial Z}$  = measurement sensitivity with respect to the total column ozone,  $Z = \Omega$ , or the surface  
242 reflectivity,  $Z = R$ , for wavelengths  $\lambda_1$  or  $\lambda_2$ .

243 If one assumes the sensitivities to the surface reflectivity,  $\partial N_{\lambda_i}/\partial R$  are wavelength independent,  
244 Eq. 5 for the triplet algorithm is similar to the Version 8 TOMS algorithm (Rodriguez et al., 2003).

245 Since the algorithm for ozone (Eqs. 8 to 10) requires the use of two or more wavelength  
246 channels, the measured counts/second for each channel must be geolocated on a common latitude  $\times$   
247 longitude grid that is accurate to 0.25 of a single pixel size. When projected on the 3-D Earth, the  
248 sampling size is about 8 km at nadir and effectively increases to 10 km when EPIC's point spread  
249 function is applied. The result for  $2 \times 2$  pixel averaging is a spatial resolution at nadir of about 18 km,  
250 which gets larger as the secant of the SLA from the nadir point. SLA is measured relative to the normal  
251 to the Earth's surface, and is  $0^\circ$  at nadir and almost  $90^\circ$  at the Earth's sunlit terminator. The radiative  
252 transfer spherical geometry correction is accurate to about  $80^\circ$  in SZA and SLA, which means that  
253 retrieved ozone values near the Earth's terminator are not accurate.

## 254 **2 Natural Color Images**

255 A typical eye response color image view of the Earth, obtained by a weighted combination of  
256 the geolocated red, green, and blue wavelength channels, is shown in Fig. 2. To produce RGB images  
257 adjusted to the human eye response, the algorithm used is a derivative of the International Commission  
258 on Illumination (CIE) process for estimating tristimulus values from calibrated instruments (Wysecki  
259 and Stiles, 1982; Broadbent, 2004; Gardner, 2007; Bodrogi and Khanh, 2012). Obtaining eye response  
260 images for EPIC's narrow band filters (Table 1) was improved by customization of the algorithm to use  
261 additional channels than just the 443, 551, and 680 nm blue, green, and red channels.

262 Because the blue 443 nm channel is not spatially averaged onboard the spacecraft, the color  
263 images have a maximum resolution of about 10 km at nadir determined by looking at the discernable  
264 width of the Nile and Amazon Rivers. The color images also give an indication of the quality of the  
265 geolocation. Errors in geolocation would appear as pink edges at the cloud boundaries, which are not  
266 present in the images in Figs. 3 or in the complete image collection on <http://epic.gsfc.nasa.gov/>.

267 Even with accurate geolocation, about 0.25 pixels (2 km), between the 4 UV channels, there is  
268 some noise introduced into ozone retrievals by small cloud edge location errors when transferring all of  
269 the native data to a common latitude and longitude grid. Ozone retrievals over almost cloud-free  
270 scenes, such as over the Saharan desert or clear-sky portions of the oceans, show much less noise than  
271 those with partial cloud cover. Since the pixel-to-pixel noise caused by misaligned cloud edges is almost  
272 random, spatial averaging to about  $50 \times 50 \text{ km}^2$  (similar to TOMS and OMPS, but coarser than OMI spatial  
273 resolution) reduces the effect of apparent noise from cloud edges. The following sections use  $25 \times 25$   
274  $\text{km}^2$  spatial averaging ( $3 \times 3$  CCD pixels), which has more spatial details and some cloud-edge noise  
275 (noise  $< 3\%$ ).

276





### 277            **3 Examples of EPIC Ozone and Reflectivity**

278            A matched pair of images for ozone and scene reflectivity LER (17 April 2016) are shown in Fig. 4  
279 with a maximum resolution of 18 km, since all UV channels involved in the ozone retrieval are  
280 downlinked from the spacecraft at a resolution of 2 x 2 onboard averaged pixels. Note that the reduced  
281 resolution hdf5 data files stored on the ground are in their original sampling density (2048 x 2048), but  
282 have reduced spatial resolution. In Fig. 4, the entire data image for ozone and the LER scene reflectivity  
283 are all at a common Universal Time (00:36 UTC or 12:36 local time at the center of the image) and  
284 encompasses local times from sunrise (west) to sunset (east) with all images rotated so that north is up.  
285 In the LER scene, a large east-west belt of clouds are visible near the equator, as are cloud plumes  
286 descending from the Arctic. The major cloud patterns change slowly, but show major seasonal changes.  
287 Figure 5 shows six additional scenes from the same day, 17 April 2016, with large cloud features  
288 associated with the Arctic region, an equatorial cloud band, and large cloud structures over the Antarctic  
289 Ocean. Figure 6 shows reflectivity measurements for 23 November 2015 with cloud features common in  
290 the Southern Hemisphere SH. The cloud band extending toward the Antarctic region from Argentina's  
291 Salado River is an example of a persistent feature that appears frequently throughout the year. In a  
292 later section, the amounts of retrieved ozone and cloud reflectivity  $0 < R_c < 1$  are used to estimate the  
293 amount of UV radiation reaching the earth's surface over snow/ice free scenes.

294            The Arctic and Antarctic ice sheets are visible after their spring equinox times, and especially in  
295 their respective late spring and summer images when the Earth's poles are tilted toward L-1 (Figs. 5 and  
296 6). In the color and LER images, clouds over ice are not readily visible because of the very high ice  
297 reflectivity providing little or no contrast with 388 nm cloud reflectivity. It is possible to obtain  
298 information about clouds over ice from the O<sub>2</sub> A-band channel at 764 nm (Fig. 7), which differentiates  
299 between reflecting surfaces that are at different altitudes because of oxygen absorption in the  
300 atmosphere. In this image, the bright white clouds (less atmospheric O<sub>2</sub> absorption) are at higher  
301 altitudes than the grey clouds, which are all higher than the ice surfaces. A quantitative analysis of cloud  
302 height and cloud-caused reduction in solar irradiance reaching the ice surface will be the subject of a  
303 future paper.

### 304            **4 Validation of EPIC Ozone Retrieval**

305            EPIC retrieved ozone can be validated by comparison with other ozone measuring satellite data  
306 (e.g., OMI, and OMPS) and by comparison with well-calibrated ground-based instruments.

307            While EPIC observes from sunrise to sunset in every image, there are only 6 to 8 useful  
308 coincidences per 24 hours with a specified ground site separated by either 68 minutes (NH summer) or  
309 110 minutes (NH winter). Coincidences at high SZA  $> 75^\circ$  are increasingly inaccurate for both satellite  
310 and ground-based retrievals. This problem is compounded for EPIC, since high SZA also implies high SLA,  
311 which increases the spherical geometry correction error. Ozone absorption and Rayleigh scattering at  
312 high SZA also prevents 317.5 nm radiances from reaching into the lower troposphere and to the surface,  
313 which is partially mitigated by having the retrieval algorithm automatically switch from 317.5 nm to 325  
314 nm at high optical depths (usually high SZA).



315 A comparison of EPIC retrieved TCO with those determined by a Pandora spectrometer  
316 instrument (#034) located at Boulder, Colorado is shown in Fig. 8. This Pandora was selected because it  
317 has been extensively compared to a well calibrated Dobson spectroradiometer and to OMI and OMPS  
318 ozone overpass data (Herman et al., 2015). The Pandora data are matched in location and time  $t_0$  to the  
319 EPIC UTC when Boulder, Colorado is in view (several times per 24 hours). Pandora ozone is averaged  
320 over  $t_0 \pm 12$  minutes. EPIC data are limited to distances within 50 km of Boulder, Colorado. Figure 8  
321 shows that EPIC and Pandora ozone amounts track each other closely during 2015 and 2016. The 2015-  
322 2016 average agreement is  $2.7 \pm 4.9$  %. There is a period in the winter of 2016 where the Pandora data  
323 quality was degraded by the presence of heavy cloud cover and in February by a mechanical problem  
324 with the Pandora sun tracker.

325 The OMI and OMPS satellites are polar orbiting with an equator crossing time of about 13:30  
326 hours local time measuring in a narrow strip on either side of the orbital track. While it is possible to  
327 compare EPIC ozone with low earth orbit satellite data, a more complete comparison can be made with  
328 the assimilated ozone product from MERRA-2, the Modern-Era Retrospective Analysis for Research and  
329 Applications, (Rotman et al., 2002) version 2 (MERRA-2, Molod et al., 2014). MERRA-2 ozone is based on  
330 Microwave Limb Sounder (MLS) and total column ozone from the Ozone Monitoring Instrument OMI on  
331 NASA's EOS *Aura* satellite. The advantage of using MERRA-2 is that the ozone field is synoptic and can be  
332 directly compared with EPIC for the same UTC (Fig. 9) over the same sunlit globe as seen by EPIC. The ozone  
333 structures seen by EPIC are all present in the MERRA-2 independent assimilation, even though there is an  
334 average offset of about 10 DU (3 %). The disagreement with EPIC is similar to the offset of MERRA-2 with  
335 other satellite data (Wargan et al., 2017). A close look at the ozone maps in Fig. 9 shows overall agreement  
336 with most features including the small region of elevated  $O_3$  over the central US. There are differences, such  
337 as the higher amount of  $O_3$  measured by EPIC over Brazil on 23 November and the structure at  $15^\circ N$  in the  
338 transition from equatorial  $O_3$  values to mid-latitude values (dark blue to light blue).

### 339 5.0 Synoptic Variation of Ozone (SVO) from Sunrise to Sunset

340 Most LEO satellite views of ozone are at almost fixed local time based on the equator crossing  
341 local solar time ( $13.5 \pm 0.8$  hours side scanning) with approximately 20 minutes local time variation from  
342 the equator to the pole. Longitudinal coverage is obtained by piecing together North-South strips  
343 obtained about 90 minutes apart. Variation that occurs on a scale less than 90 minutes cannot be seen  
344 from a polar orbiting LEO satellite, nor can variation from different local times of the day. EPIC observes  
345 from close to sunrise and sunset with local solar noon near the center of the data set as shown in Fig.  
346 10. The exact position of noon in the EPIC images depends on the location of EPIC in its orbit relative to  
347 the Earth-Sun line. The longitude resolution is approximately  $0.25^\circ$  at the center of the FOV, which  
348 corresponds to a time resolution of about 1 minute. The resolution decreases as the secant of the angle  
349 from the center (e.g., 2 minutes or  $0.5^\circ$  at  $60^\circ$  from the center). A limitation in the EPIC observations  
350 occurs at high SZA and high SLA. As can be seen in Fig. 10, ozone values near the morning terminator are  
351 probably too low compared to the middle longitude values. These retrieval errors are partly caused by  
352 the effects of spherical geometry that are not properly represented in the TOMRAD radiative transfer  
353 calculations.



354 The view of the EPIC instrument from sunrise to sunset at fixed UTC is not the diurnal variation  
355 that an instrument on the ground would see from sunrise to sunset. For the ground-based Pandora  
356 instrument, the observed changes throughout the day from sunrise to sunset are at varying UTC every  
357 80 seconds. Compared to the ground-based viewpoint, EPIC obtains data for a fixed geographic location  
358 every 68 minutes UTC in NH daytime summer and every 110 minutes in NH daytime winter.

### 359 5.1 Southern Hemisphere SH Late Spring 23 November 2015 :

360 To illustrate the SH synoptic change in ozone, Figs. 10 and 11 show the diurnal (longitudinal)  
361 variation of ozone centered on the South American continent on 23 November 2015 at 16:20 UTC. The  
362 local time varies from early morning (06:20,  $-150^{\circ}$  longitude) to late-afternoon (16:20,  $0^{\circ}$  longitude). At  
363 high southern latitudes,  $60^{\circ}\text{S}$  and  $70^{\circ}\text{S}$ , the late spring (23 November) residue of 2015 Antarctic ozone  
364 hole is clearly visible in the ozone map image (Fig. 10). Figure 11 shows details of the ozone amounts in  
365 specified latitude bands ( $\pm 0.125^{\circ}$  wide) in the Southern Hemisphere sampled every  $5^{\circ}$  degrees from  $0^{\circ}$   
366 to  $70^{\circ}\text{S}$ . Solar zenith angles are limited to the range  $\pm 70^{\circ}$  to avoid high latitudes and longitudes near  
367 sunrise or sunset where spherical geometry effects become important. This particular example (Fig. 11)  
368 is from one image centered over South America (Fig. 10). For 23 November there are 15 more  
369 overlapping images covering the entire  $360^{\circ}$  of longitude that could be combined to produce a complete  
370 composite global map of ozone at 15 different UTCs. In the NH summer there would be 22 images per  
371 day. A composite ozone map of this kind would no longer be synoptic, since overlapping data are  
372 averaged, but would now be similar to the joined data strips from OMI or OMPS.

373 Figure 11 contains the data points from a  $0.25^{\circ} \times 0.25^{\circ}$  average within each  $5^{\circ}$  latitude band  $L$   
374 shown as light grey dots. The dark lines are a Lowess(0.05) fit (locally weighted least squares fit to 5 % of  
375 the data, (Cleveland, 1981)), which corresponds to approximately a 30 minute time average ( $7.5^{\circ}$   
376 Longitude). The largest apparent scatter from the Lowess fit occurs at  $L = 0.125^{\circ}\text{S}$ , which amounts to a  
377 longitudinal standard deviation from the mean of  $\pm 4$  DU or  $\pm 1.5$  %. The equatorial bands ( $0^{\circ}\text{S}$  to  $20^{\circ}\text{S}$ )  
378 shows considerable longitudinal change (10–20 % from  $L = 0$ – $40^{\circ}\text{S}$  rising to 75 % at  $L = 70^{\circ}\text{S}$ ,  
379 approximately as  $\text{TCO} = 16.063 + 0.56L + 0.02L^2$ ). Most of the observed changes are dynamically driven,  
380 since the photochemistry involved in the stratosphere (20 - 25 km altitude) is too slow to produce such  
381 large changes with changing SZA. Southward of  $45^{\circ}\text{S}$ , the effects of the remaining ozone hole depletion  
382 (dark blue in Fig. 10), which is still present in November, appear at  $-50^{\circ}$  longitude as indicated in Fig. 11.

### 383 5.2 Northern Hemisphere NH Summer Solstice 21 June 2016:

384 An example is provided for the ozone retrievals obtained on 21 June 2016 at 18:41 UTC that is  
385 approximately centered over North America (Fig. 12). Since this is Northern Hemisphere summer  
386 solstice, corresponding to the sun being nearly overhead at  $23^{\circ}\text{N}$ , the latitude range available for  
387 retrieving ozone extends over the North Pole. Figure 13 contains ozone retrievals in  $0.25^{\circ}$  wide latitude  
388 bands similar to Fig. 11. Unlike the SH 23 November 2015 example, there is only moderate longitudinal  
389 (diurnal) variability in ozone amount for latitudes between  $0^{\circ}$  and  $15^{\circ}\text{N}$ . However, there is a clear wave  
390 structure in the  $20^{\circ}\text{N}$  to  $25^{\circ}\text{N}$  bands with a periodicity of approximately  $35^{\circ}$  longitude (2.3 hours) and  
391 again in the  $40^{\circ}\text{N}$  to  $60^{\circ}\text{N}$  bands that are not obvious in the global map (Fig. 12).



392 The dynamical effects on ozone in the NH mid-latitudes are quite different than their  
393 counterparts in the SH, where the NH mid-latitude behavior ( $30^{\circ}\text{N}$ – $35^{\circ}\text{N}$ ) is clearly separated from  
394 equatorial and high latitude bands with an increase in ozone amount from about 280 DU to about 350  
395 DU, which is larger than a similar increase in the SH. There is an ozone periodicity of approximately  $38^{\circ}$   
396 longitude (2.5 hours) at  $30^{\circ}\text{N}$ – $35^{\circ}\text{N}$  midday and a longer longitudinal period  $73^{\circ}$  (4.9 hours) in the  
397 morning. At higher latitudes,  $35^{\circ}\text{N}$ – $55^{\circ}\text{N}$ , the variability is more pronounced with an approximate  
398 period of  $55^{\circ}$  (3.6 hours). In the bands from  $55^{\circ}\text{N}$ – $70^{\circ}\text{N}$  the variability is reduced and the ozone amount  
399 falls from mid-latitude values of about 350 DU to below 300 DU. The wave structure varies throughout  
400 the year in both hemispheres.

### 401 **5.3 Northern and Southern Hemisphere 17 April 2016 18:35 UTC**

402 Figure 5-5 shows the ozone retrieval for the sunlit globe on 17 April 2016 at 18:36 UTC about 1  
403 month from the March equinox including large plumes of elevated ozone amounts (450 DU) extending  
404 from high latitudes into mid-latitudes where the usual ozone amount is about 350 DU. For the SH (Fig. 5-  
405 5), polar ozone variability (280-320 DU) is relatively small compared to November 23 (Fig. 10). There is  
406 wave structure (Fig. 15) between  $30^{\circ}\text{S}$  and  $40^{\circ}\text{S}$  with a periodicity of about 4 hours ( $60^{\circ}$  longitude) (see  
407 also Schoeberl and Kreuger, 1983). The dip in  $\text{O}_3$  amount at  $77^{\circ}\text{W}$  to  $67^{\circ}\text{W}$  and  $10^{\circ}\text{S}$  to  $25^{\circ}\text{S}$   
408 corresponds to the Andes Mountains in Peru, Bolivia, and Chile. While the SZA range is limited to  $\pm 70^{\circ}$ ,  
409 the SLA reaches more than  $80^{\circ}$  at low latitudes for longitudes between  $40^{\circ}\text{S}$  and  $20^{\circ}\text{S}$  introducing  
410 spherical geometry correction errors that increase towards sunset near  $20^{\circ}\text{W}$ . The errors appear as  
411 apparent increases in  $\text{O}_3$  amount. At higher latitudes, the SLA is in the middle  $70^{\circ}\text{s}$  when the SZA is  $70^{\circ}$ .  
412 The high SLA error is present in both hemispheres for observations near equinox.

413 The NH shows little variability in the equatorial region ( $0$ – $25^{\circ}\text{N}$ ) with a mean value of about 260  
414 DU (Fig. 16). The SLA error is present for latitudes between  $0$  and  $15^{\circ}\text{N}$  and  $0$  and  $15^{\circ}\text{S}$  that appears as  
415 an elevated ozone amount at longitudes east of  $50^{\circ}\text{W}$ . Mid-latitudes ( $30^{\circ}\text{N}$  to  $40^{\circ}\text{N}$ ) show a wave  
416 structure that is approximately  $37^{\circ}$  apart (2.5 hours) at  $35^{\circ}\text{N}$ . A similar structure occurs in the SH with a  
417 period of about 4.5 hours. There is an ozone maximum (red area in Fig. 14 about 450 DU) near  $140^{\circ}\text{W}$   
418 extending from  $60^{\circ}\text{N}$  to  $35^{\circ}\text{N}$ , very high ozone amounts in the Arctic region, and a high ozone patch  
419 over the central US ( $35^{\circ}\text{N}$  to  $45^{\circ}\text{N}$  and  $104^{\circ}\text{W}$ ) peaking at 420 DU ( $40^{\circ}\text{N}$  and  $104^{\circ}\text{W}$ ), which probably  
420 corresponds to a region of high atmospheric pressure.

### 421 **6.0 Estimating Erythemal Irradiance at the Earth's Surface**

422 The unique observing geometry of DSCOVR/EPIC permit the use of synoptic ozone and cloud  
423 reflectivity data to be used to compute the diurnal variation of UV irradiance from sunrise to sunset for  
424 any point on the illuminated earth observed by EPIC. Previous calculations from satellite data used  
425 cloud cover and ozone from 13:30 and assumed it applied to local noon. The assumption is usually  
426 adequate for slowly varying ozone, but not for estimating the effects of more rapidly varying cloud  
427 cover. The following paragraphs discuss the calculation of erythemal irradiance, a spectrally weighted  
428 mixture of UV wavelengths used as a measure of skin reddening and potential sunburn from exposure to  
429 sunlight.



430 Erythemal irradiance  $E_0(\text{SZA } \theta, \text{ altitude } Z)$  at the earth surface ( $\text{watts/m}^2$ ) is defined in terms of  
 431 a wavelength dependent weighted integral over a specified weighting function  $A(\lambda)$  times the incident  
 432 solar irradiance  $I(\lambda, \theta, \Omega, C_T)$  ( $\text{Watts/m}^2$ ) (Eq. 11) at the Earth's surface. The erythemal weighting function  
 433  $\text{Log}_{10}(A_{\text{ERY}}(\lambda))$  is given by the standard Erythemal fitting function shown in Eq. 12 (McKinley and Diffey,  
 434 1987). Tables of radiative transfer solutions for  $D_E = 1 \text{ AU}$  are generated for a range of sza ( $0 < \theta < 90^\circ$ ),  
 435 for ozone amounts  $100 < \Omega < 600 \text{ DU}$ , and terrain heights  $0 < Z < 5 \text{ km}$  using the TUV DISORT radiative  
 436 transfer model as described in Herman (2010) for erythemal and other action spectra (e.g., plant  
 437 growth, vitamin D production, cataracts, etc.).

$$E_0(\theta, \Omega, C_T) = \int_{250}^{400} I(\lambda, \theta, \Omega, C_T) A(\lambda) d\lambda \quad (11)$$

$$\begin{aligned} 250 < \lambda < 298 \text{ nm} & \quad \text{Log}_{10}(A_{\text{ERY}}) = 0 \\ 298 < \lambda < 328 \text{ nm} & \quad \text{Log}_{10}(A_{\text{ERY}}) = 0.094 (298 - \lambda) \\ 328 < \lambda < 400 \text{ nm} & \quad \text{Log}_{10}(A_{\text{ERY}}) = 0.015 (139 - \lambda) \end{aligned} \quad (12)$$

438 Equation 11 can be accurately approximated by the power law form (Eq. 13), where  $U(\theta)$  and  $R(\theta)$   
 439 are fitting coefficients to the radiative transfer solutions in the form of rational fractions. Rational  
 440 fractions were chosen because they tend to behave better at the ends of the fitting range than  
 441 comparable fitting accuracy polynomials.

$$E_0(\theta, \Omega, C_T) = U(\theta) (\Omega/200)^{-R(\theta)} C_T \quad (13)$$

$$U(\theta) \text{ or } R(\theta) = (a+c\theta^2+e\theta^4)/(1+b\theta^2+d\theta^4+f\theta^6) \quad r^2 > 0.9999 \quad (14)$$

$$C_T = (1-\text{LER})/(1-R_G) \text{ where } R_G \text{ is the reflectivity of the surface} \quad (15)$$

$$E(\theta, \Omega, Z) = E_0(\theta, \Omega) H(\theta, \Omega, z) \quad (16)$$

$$H(\theta, \Omega, Z) = 1 + (0.04652 Z_{\text{km}} + 0.00496) (-0.07033 (\Omega/200) + 1.12303) G(\theta) \quad (17)$$

$$G(\theta) = g + h\theta + i\theta^2 + j\theta^3 + k\theta^4 \quad (18)$$

The coefficients  $a, b, c, d, e, f, g, h, j,$  and  $k$  are in Tables A-1 and A-2 in the appendix

442 The  $E_0$  solutions to the radiative transfer calculations can be accurately reproduced by a relatively  
 443 simple functional form (Eqs. 13 to 15) with the coefficients given in Table A-1. These are the same  
 444 coefficients given in Herman (2010) along with other biological action spectra weighting functions,  $H(z, \theta)$   
 445 is a function representing the increase in  $E(\theta, \Omega, Z)$  with altitude per km, and  $C_T$  is the cloud transmission  
 446 function (Eq. 15) estimated from the retrieved LER derived by assuming that the cloud-ground system  
 447 can be approximated by a two-layer Stokes problem (elevated cloud and surface) with atmospheric  
 448 effects between the cloud bottom and the surface neglected (Herman et al., 2009).  $r^2$  is a measure of  
 449 the correlation of the  $E_0$  data points with the fitting function. Eqs. 13 to 18 are for an Earth-Sun distance  
 450 of 1 AU.



451 For  $E_0$  The fitting residual is less than  $\pm 0.001 \text{ W/m}^2$  compared to the worst case when  $E_0(50^\circ,$   
452  $200) = 0.15 \text{ W/m}^2$  (Herman, 2010). When height effects are included  $E(\theta, \Omega, Z) = E_0(\theta, \Omega) H(\theta, \Omega, Z)$ ,  
453 where  $H(\theta, \Omega, Z)$  is a fitting polynomial (Eq. 17) to the downward irradiance at 0, 1, 2, 3, 4, and 5 km  
454 based on results from the radiative transfer calculation. The increase of erythemal irradiance with  
455 altitude has an SZA dependence given by  $G(\theta)$ , which increases with  $\theta$  until  $\theta$  is approximately  $60^\circ$ , and  
456 then  $G(\theta)$  decreases.

457 The height dependence of  $E(\theta, \Omega, Z)$  is similar to that derived by Chubarova et al. (2016) for low  
458 aerosol amounts. When absorbing aerosols have a significant optical depth, Chubarova et al. (2016)  
459 derived a multiplicative correction term to  $E(\theta, \Omega, Z)$  for a wide variety of conditions.

460

461 When Eq. 13 is applied to the ozone and LER data described in previous sections, the global  
462 erythemal irradiance at the ground can be obtained after correction for the Earth-Sun distance  $D_E$  in a  
463 manner similar to Eq. 1, where  $D_E$  in AU can be approximated by (Eq. 19),  
464

$$D_E = 1 - 0.01672 \cos(360 (\text{day\_of\_year} - 4)/365.25) \quad (19)$$

465

466 An example of  $E(\theta, \Omega, Z)$  is shown in Fig. 17 for 17 April 2016 at 18:35 UTC. Local noon is near  
467 the center of the image with sunrise to the left (west) and sunset to the right (east). For this date, the  
468 sun is overhead just north of the equator producing very high values of Erythemal irradiance  $E(\theta, \Omega, Z)$   
469 corresponding to a UV index, UVI, of 13 at sea level in the Pacific Ocean ( $\text{UVI} = 40 E(\theta, \Omega, Z)$ ). The UVI  
470 scale was designed for sea level mid latitudes ranging from 0 to 10 to provide public health warnings  
471 (e.g. for UVI = 8). Somewhat higher values are seen in the Sierra Nevada Mountains in Mexico near  
472  $20^\circ\text{N}$ . This particular day is relatively cloud free over most of South America except for clouds over  
473 southern Brazil extending into Paraguay and other small patches of clouds. For the erythemal irradiance,  
474 the presence of clouds reduces the amount of UV reaching the ground (blue color with a UV index of  
475 less than 4).

476

477 The increase with altitude is much more pronounced during the summer months over the Andes  
478 Mountains reaching above 4 km (over 13,000 feet). Figures 18 and 19 show the large increases with  
479 altitude over the Andes Mountains for 23 November 2015, with the sun nearly overhead at  $20^\circ\text{S}$   
480 latitude. Here the UV index ranges from 16 to 18, which agrees with previous ground-based  
481 measurements in this region (Cede et al., 2002). Any significant unprotected exposure to these levels of  
482 UV would lead to severe sunburn and eye damage. On a completely clear day the UV index would be  
483 even higher than 18. Figure 19 is a longitudinal slice through the UV data in Fig. 18 at  $20^\circ\text{S}$ . The figure  
484 shows the longitudinal variation  $E(\theta, \Omega, Z)$  as a function of local time, the effect of light clouds on the  
485 eastern side of the Andes Mountains, and the sharp reduction at  $50^\circ\text{W}$ .

486

487 Figure 20 shows the erythemal irradiance computed for 21 June 2016 centered over the US and  
488 Central America. The sun is overhead at  $23.3^\circ\text{N}$  latitude. In the clear regions not covered with light  
489 clouds, the UV index reaches about 12 extending from an area in the Pacific Ocean at  $15^\circ\text{N}$  up into the  
490 US mid-west, Rocky Mountains, Utah and New Mexico. The eastern US has a lower UV index of about 8.



491 The extended scale of this map (UVI = 0 to 20) is too coarse to see the variation with latitude on the east  
492 coast.

493

494 Similarly, Fig. 21 shows high values of Erythema irradiance in the Himalayan Mountains on June  
495 21, 2016 with peak UV index of about 15 even in the presence of partial cloud cover that reflects a  
496 portion of the incident solar flux back to space. The effect of cloud cover can be seen in Fig. 22, which is  
497 a longitudinal slice through the irradiance values associated with the latitude at 32°N. In the absence of  
498 clouds, the peak value of the UV index would be close to 20. Even with cloud cover, the UV index  
499 reached 15, which is twice the value of a typical cloudless summer case in the US at comparable  
500 latitude.

## 501 **7.0 Summary**

502 The DSCOVR/EPIC 10-filter Spectroradiometer (317.5 to 780 nm) makes measurements of the  
503 rotating sunlit face of the earth from the Lagrange-1 point located  $1.5 \times 10^6$  km from the earth with a  
504 maximum resolution of  $10 \times 10$  km<sup>2</sup> for 443 nm at the sub-satellite point. The other 9 channels have  $18 \times$   
505  $18$  km<sup>2</sup> resolution. The key difference between EPIC and LEO satellites is EPIC's ability to measure the  
506 whole sunlit earth (sunrise to sunset) at the same UTC (synoptic measurements) every 68 or 110  
507 minutes depending on the season at the Wallops Island, Virginia data receiving station. EPIC ozone  
508 retrievals have been compared successfully to both ground-based Pandora spectrometer instruments  
509 and to the MERRA-2 satellite data assimilation model for the same UTC observed by EPIC. EPIC's  
510 synoptic measurements insure that the ozone amounts, cloud reflectivity, and aerosol amounts that are  
511 used to estimate UV irradiance are the proper values for each time of the day. EPIC has been making  
512 measurements since June 15, 2015 with no evidence of significant degradation relative to LEO satellites  
513 observing the same scene at the same angles. EPIC has obtained ozone and reflectivity data multiple  
514 times per 24 hours for over two years that can be used to more accurately estimate the health effects  
515 from continuous or periodic exposure during any day to UV radiation reaching the ground including the  
516 effects of cloud cover and altitude.

517

518

519

520

521

522

523

524



525 **Appendix**

526 Figure A1 illustrates the orbit of the DSCOVR spacecraft following the earth in its orbit about the  
 527 sun.

528

Table A-1 Coefficients  $R(\theta)$  and scaling coefficient  $U(\theta)$  for  $0 < \theta < 80^\circ$   
 and  $100 < \Omega < 600$  DU for  $E(\Omega, \theta) = U(\theta) (\Omega/200)^{-R(\theta)}$  ( $1.0E10 = 1.0 \times 10^{10}$ )

$$U(\theta) \text{ or } R(\theta) = (a+c\theta^2+e\theta^4)/(1+b\theta^2+d\theta^4+f\theta^6) \quad r^2 > 0.9999$$

Action Spectra	$U(\theta)$ (watts/m <sup>2</sup> )	$R(\theta)$
CIE Erythemat $U_{ERY}$ & $R_{ERY}$	a= 0.4703918683355716 b= 0.0001485533527344676 c= -0.0001188976502179551 d= 1.915618238117361E-08 e= 7.693069873238405E-09 f= 1.633190561844982E-12	a= 1.203020609002682 b= -0.0001035585455444773 c= -0.00013250509260352 d= 4.953161533805639E-09 e= 1.897253186594168E-09 f= 0.0

Table A-2 Solar Zenith angle function  $G(\theta)$  used in Eq. 18

$$G(\theta) = g+h\theta+i\theta^2+j\theta^3+k\theta^4$$

g= 0.9996074048174048	j= 1.412462444962443E-06
h= 0.0001453776871276851	k= -2.037907925407924E-08
i= 2.806514180264192E-05	

529

530

531

532

533

534

535

536

537

538





539 **References**

540 Bodrogi, Peter and Tran Quoc Khanh, Illumination, Color and Imaging: Evaluation and Optimization of  
541 Visual Displays, Wiley-VCH Verlag GmbH & Co. KGaA. 2012.

542

543 Brion, J., Chakir, A., Daumont, D., Malicet, J., and Parisse, C.: High-resolution laboratory absorption cross  
544 section of O<sub>3</sub>. Temperature effect, Chem. Phys. Lett., 213, 610–612, 1993.

545

546 Brion, J., Chakir, A., Charbonnier, J., Daumont, D., Parisse, C., and Malicet, J.: Absorption spectra  
547 measurements for the ozone molecule in the 350–830 nm region, J. Atmos. Chem., 30, 291–299, 1998.

548 Broadbent, Arthur D. A critical review of the development of the CIE1931 RGB color-matching functions,  
549 Color Research & Applications. 29 (4): 267–272. doi:10.1002/col.20020, 2004

550

551 Cariolle, D., and M. Déqué (1986), Southern hemisphere medium-scale waves and total ozone  
552 disturbances in a spectral general circulation model, J. Geophys. Res., 91(D10), 10825–10846,  
553 doi:[10.1029/JD091iD10p10825](https://doi.org/10.1029/JD091iD10p10825) 1986.

554

555 Caudill, T.R., D.E. Flittner, B.M. Herman, O. Torres, and R.D. McPeters, Evaluation of the pseudo-  
556 spherical approximation for backscattered ultraviolet radiances and ozone retrieval, J. Geophys. Res.,  
557 102, 3881-3890, 1997.

558

559 Cede, A., E. Luccini, R.D. Piacentini, L. Nuñez, and M. Blumthaler, Monitoring of Erythemal Irradiance in  
560 the Argentine Ultraviolet Network, J. Geophys. Res., 107 (D13), 10.1029/2001JD001206, 2002.

561

562 Cleveland, William S., LOWESS: A program for smoothing scatterplots by robust locally weighted  
563 regression. The American Statistician. 35 (1): 54. [JSTOR 2683591](https://www.jstor.org/stable/2683591). doi:10.2307/2683591, 1981.

564

565 Daumont, D., Brion, J., Charbonnier, J., and Malicet, J.: Ozone UV spectroscopy I: Absorption cross-  
566 sections at room temperature, J. Atmos. Chem., 15, 145–155, 1992.

567

568 Dobber, M., Voors, R., Dirksen, R., Kleipool, Q., and Levelt, P., 2008, The high resolution solar reference  
569 spectrum between 250 and 550 nm and its application to measurements with the Ozone Monitoring  
570 Instrument. Solar Phys., 249, 281–291, 2008.



571

572 Gardner, James L., Comparison of Calibration Methods for Tristimulus Colorimeters, Journal of Research  
573 of the National Institutes of Standards and Technology. **112** (3): 129–138. [doi:10.6028/jres.112.010](https://doi.org/10.6028/jres.112.010),  
574 2007.

575

576 Herman, J.R., G. Labow, N.C. Hsu, D. Larko (2009), Changes in Cloud Cover (1998-2006) Derived From  
577 Reflectivity Time Series Using SeaWiFS, N7-TOMS, EP-TOMS, SBUV-2, and OMI Radiance Data, J.  
578 Geophys. Res., 114, D01201, doi:10.1029/2007JD0008, 2009.

579

580 Jaross, G., P. K. Bhartia, G. Chen, M. Kowitt, M. Haken, Z. Chen, P. Xu, J. Warner, and T.  
581 Kelly (2014), OMPS Limb Profiler instrument performance assessment, J. Geophys. Res.  
582 Atmos., 119, 4399–4412, doi:[10.1002/2013JD020482](https://doi.org/10.1002/2013JD020482), 2014.

583

584 Madronich, S., McKenzie, R.L., Björn, L.O. and Caldwell, M.M. (1998), "Changes in biologically active  
585 ultraviolet radiation reaching the Earth's surface," *Photochem. Photobiol.* **46**, 5-19, 1998.

586

587 Malicet, J., Daumont, D., Charbonnier, J., Chakir, C., Parisse, A., and Brion, J.: Ozone UV Spectroscopy. II:  
588 Absorption cross sections and temperature dependence, *J. Atmos. Chem.*, 21, 263–273, 1995.

589

590 Marshak, A., T., Várnai, and A., Kostinski (2017), Terrestrial glint seen from deep space: Oriented ice  
591 crystals detected from the Lagrangian point, *Geophys. Res. Lett.*, 44, doi:10.1002/2017GL073248, 2017.

592

593 McKinley, A. F., and B. L. Diffey (1987), A reference action spectrum for ultraviolet induced erythema in  
594 human skin, in *Human Exposure to Ultraviolet Radiation: Risks and Regulations*, edited by W. R.  
595 Passchier and B. F. M. Bosnjakovic, pp. 83 – 87, Elsevier, Amsterdam, 1987.

596

597 Molod, A., Takacs, L., Suarez, M., and Bacmeister, J., 2014: Development of the GEOS-5 atmospheric  
598 general circulation model: evolution from MERRA to MERRA-2, *Geosci. Model Dev. Discuss.*, 7, 7575-  
599 7617, doi:10.5194/gmdd-7-7575-2014.

600

601 Rodriguez, Juan V., ; Colin J. Seftor ; Charles G. Wellemeyer and Kelly Chance (2003), "An overview of the  
602 nadir sensor and algorithms for the NPOESS ozone mapping and profiler suite (OMPS)", *Proc. SPIE* 4891,



603 Optical Remote Sensing of the Atmosphere and Clouds III, 65 (April 9, 2003); doi:10.1117/12.467525;  
604 <http://dx.doi.org/10.1117/12.467525>, 2003.

605

606 Rotman, D.A., J.R. Tannahill, D.E. Kinnison, P.S. Connell, D. Bergmann, D. Proctor, J.M. Rodriguez, S.J.  
607 Lin, R.B. Rood, M.J. Prather, P.J. Rasch, D.B. Considine, R. Ramaroson, S.R. Kawa (2001), The Global  
608 Modeling Initiative assessment model: Model description, integration and testing of the transport shell,  
609 J. Geophys. Res., 106, 1669-1691, 2001.

610

611 Schoeberl, M.A. and A. J. Krueger, Medium Scale Disturbances in Total Ozone During Southern  
612 Hemisphere Summer," *Bull. Amer. Met. Soc.*, 1358, 1983.

613

614 Tzortziou, M., J. R. Herman, A. Cede, and N. Abuhassan (2012), High precision, absolute total column  
615 ozone measurements from the Pandora spectrometer system: Comparisons with data from a Brewer  
616 double monochromator and Aura OMI, J. Geophys. Res., 117, D16303, doi:10.1029/2012JD017814,  
617 2012.

618

619 Wargan, Krzysztof, Gordon Labow and Stacey Frith, Steven Pawson, Nathaniel Livesey, Gary Partyka,  
620 Journal of Climate 30, DOI: <http://dx.doi.org/10.1175/JCLI-D-16-0699.1>, 2017.

621

622 Wyszecki, Gunther and W. S. Stiles, Color Science: Concepts and Methods, Quantitative Data and  
623 Formulae, 2nd Edition, ISBN: 978-0-471-39918-6, John Wiley and Sons, 1982.

624



625 **Tables**

Table 1 Exposure Times for viewing the Earth and Full Moon (Earth side view)

Wavelength	Earth Exposure (ms)	Full Moon Exposure(ms)	Filter Width (nm FWHM)
317.5	654	2500	1
325	442	500	1
340	67	92	3
388	87	95	3
443	28	100	3
551	22	70	3
680	33	105	1.7
688	75	224	0.6
764	101	250	1.7
779.5	49	180	2

626

627



628

Table 2  $\pi K_M$  on 1 January 2016

Irradiance at 1 AU

629

M	$\lambda$ (nm)	$\pi K_{MO}$	$S_M$ (mW/m <sup>2</sup> /nm)
---	----------------	--------------	-------------------------------

630

1	317.478	1.216E-04	819.0
---	---------	-----------	-------

631

2	325.035	1.111E-04	807.7
---	---------	-----------	-------

632

3	339.858	1.975E-05	995.8
---	---------	-----------	-------

633

4	387.923	2.685E-05	1003.
---	---------	-----------	-------

634



Table A1 Coefficients  $R(\theta)$  and scaling coefficient  $U(\theta)$  for  $0 < \theta < 80^\circ$   
and  $100 < \Omega < 600$  DU for  $E(\Omega, \theta) = U(\theta) (\Omega/200)^{-R(\theta)}$  ( $1.0E10 = 1.0 \times 10^{10}$ )

$$U(\theta) \text{ or } R(\theta) = (a + c\theta^2 + e\theta^4) / (1 + b\theta^2 + d\theta^4 + f\theta^6) \quad r^2 > 0.9999$$

Action Spectra	$U(\theta)$ (watts/m <sup>2</sup> )	$R(\theta)$
CIE Erythemat $U_{ERY}$ & $R_{ERY}$	a= 0.4703918683355716 b= 0.0001485533527344676 c= -0.0001188976502179551 d= 1.915618238117361E-08 e= 7.693069873238405E-09 f= 1.633190561844982E-12	a= 1.203020609002682 b= -0.0001035585455444773 c= -0.00013250509260352 d= 4.953161533805639E-09 e= 1.897253186594168E-09 f= 0.0

635

636



Table A2 Solar Zenith angle function  $G(\theta)$  used in Eq. 18

$$G(\theta) = g+h\theta+i\theta^2+j\theta^3+k\theta^4$$

$$g= 0.9996074048174048$$

$$h= 0.0001453776871276851$$

$$i= 2.806514180264192E-05$$

$$j= 1.412462444962443E-06$$

$$k= -2.037907925407924E-08$$

637

638



639 **Figure Captions**

640 f01 Filter transmission functions (percent) for the 10 EPIC wavelengths

641 f02 Normalized calibration functions referenced to its value at 4 Jan 2016 when  $D_e = 1$  au. Average rate  
642 of increase is 0.016 per year.

643 f03 Natural Color EPIC Earth images from June 6 and December 6, 2016 showing the field of view during  
644 the respective hemispheric summers. In both of these images, 6-months apart, the EPIC orbit is to the  
645 west of the Earth-Sun line causing the west side of the globe (sunrise) to appear brighter than the east  
646 side (sunset). Notice the bright specular reflection over Argentina, South America embedded within a  
647 cloud feature. This is thought to be from ice crystals in high clouds (Marshak et al., 2017).

648 f04 EPIC retrieved ozone and LER values for April 17, 2016 at 00:36 UTC. The ozone scale is from 100 to  
649 500 DU, and the LER scale is from 0 to 100 percent.

650 f05 LER at six sequential UTC 0:36, 2:24, 4:12, 6:00, 7:48, and 9:36 from 17 April 2017 showing clouds in  
651 the arctic region as the earth rotates in EPIC's field of view.

652 f06 Cloud formations from 23 Nov 2015 showing cloud cover in the Southern Hemisphere and near  
653 Antarctica at 6 different UTC's, 10:56, 12:44 14:32, and 16:20, 14:32, 18:09, and 19:57.

654 f07 O<sub>2</sub> A-band View of Antarctica on December 6, 2015 showing clouds over ice. The white bright clouds  
655 are at higher altitudes than the dull grey clouds because of a combination of less oxygen absorption and  
656 higher optical depth.

657 f08 Daily O<sub>3</sub> data for EPIC (red) and Pandora (Grey) 2015 - 2016. Left: EPIC ozone data compared to  
658 Pandora retrievals at Boulder Colorado. Right: Percent difference between EPIC and Pandora.

659 f09 Comparison of EPIC total column ozone with the MERRA-2 assimilation model ozone.

660 f10 Global image of ozone field for Fig. 11 for 23 Nov 2015 at 16:20 UTC

661 f11 Longitudinal or diurnal variation of ozone for the Southern Hemisphere every 5° degrees from 0° to  
662 70S° for 23 Nov 2015 at 16:20 UTC. The grey points are the individual data points in the band. The solid  
663 lines are a Lowess(0.05) fit to the data points representing a solar time average from 0.6 to 0.7 hours  
664 depending on latitude. The SZA is limited to  $\pm 70^\circ$ . Longitude = 0 Corresponds to 16:20 local time and  
665 longitude = -150 corresponds to 06:20 local time.

666 f12 Global image of ozone field for Fig. 13 for 21 June 2016 at 18:41 UTC

667 f13 Longitudinal or diurnal variation of ozone for the Northern Hemisphere every 5° from 0° to 70° for  
668 21 June 2016 at 18:41 UTC. The grey bands are the individual data points in the band. The solid lines are  
669 a Lowess(0.05) fit to the data points representing a solar time average from 0.6 to 0.7 hours depending  
670 on latitude. The SZA is limited to  $\pm 70^\circ$ . Longitude = 0 Corresponds to 18:41 local time and longitude = -  
671 180 corresponds to 06:41 local time.



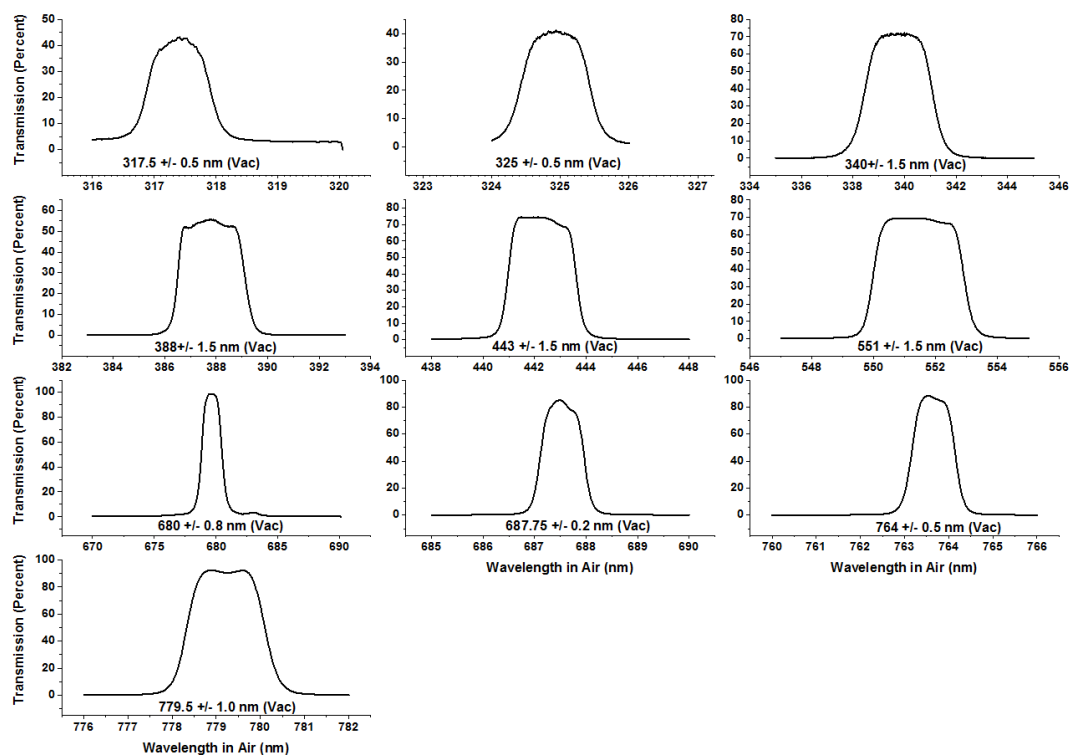


- 672 f14 Global image of ozone field for Figs. 15 and 16 for 17 April 2016 at 18:36 UTC.
- 673 f15 Southern Hemisphere: Solid lines are approximately 30 minute averages in solar time at 18:38 UTC  
674 on 17 April 2016 for ozone variation between  $0^{\circ}$  and  $55^{\circ}$ S latitude in  $0.25^{\circ}$  latitude bands for 17 April  
675 2016 at 17:36 UTC.
- 676 f16 Northern Hemisphere: Solid lines are approximately 30 minute averages in solar time at 18:38 UTC  
677 on 17 April 2016 for ozone variation between  $0^{\circ}$  and  $75^{\circ}$ N latitude in  $0.25^{\circ}$  latitude bands for 17 April  
678 2016 at 17:36 UTC.
- 679 f17 Erythemal irradiances calculated from Eq. 13 and from the EPIC ozone and LER data obtained on  
680 April 17, 2016 at 18:35 UTC. The scale shows both the irradiance values in  $W/m^2$  and the UV index  
681 ranging from 0 to 20. This scene is centered over the Pacific Ocean and shows a peak UV index of about  
682 15. Since this period is close to equinox, the sun is nearly overhead just north of the equator with solar  
683 noon at  $98.75^{\circ}$ W longitude and overhead near  $10^{\circ}$ N.
- 684 f18 Erythemal irradiances centered over South America on November 23, 2015 at 16:19 UTC showing  
685 extremely high values in the Andes Mountains in Peru, Bolivia, and Chile corresponding to a UV index  
686 greater than 20. Local solar noon is at  $64.75^{\circ}$ W and overhead near  $20^{\circ}$ S.
- 687 f19 Erythemal Irradiances in a longitudinal slice at  $20^{\circ}$ S through a peak occurring in the Andes  
688 mountains. Local noon is at  $64.75^{\circ}$ W.
- 689 f20 Erythemal irradiances centered over the United States on June 21, 2016 showing high values over  
690 the Rocky Mountains and a portions of the Sierra Nevada Mountains. The UV index reaches about 15.  
691 Local solar noon is at  $99.75^{\circ}$ W and overhead near  $23.3^{\circ}$ N.
- 692 f21 Erythemal UV irradiances centered over the Indian Ocean on June 21, 2016 showing high values over  
693 the Himalayan Mountains with the UV index exceeding 14. UV levels are moderated by partial cloud  
694 cover reflection of radiation back to space. Solar noon is at  $80.25^{\circ}$ E.
- 695 f22 Erythemal Irradiances in a longitudinal slice at  $32^{\circ}$ N through a portion of the Himalayan mountains.  
696 Local solar noon is at  $80.25^{\circ}$ E.
- 697 fA1 An illustration of DSCOVR's Lagrange-1 orbit
- 698



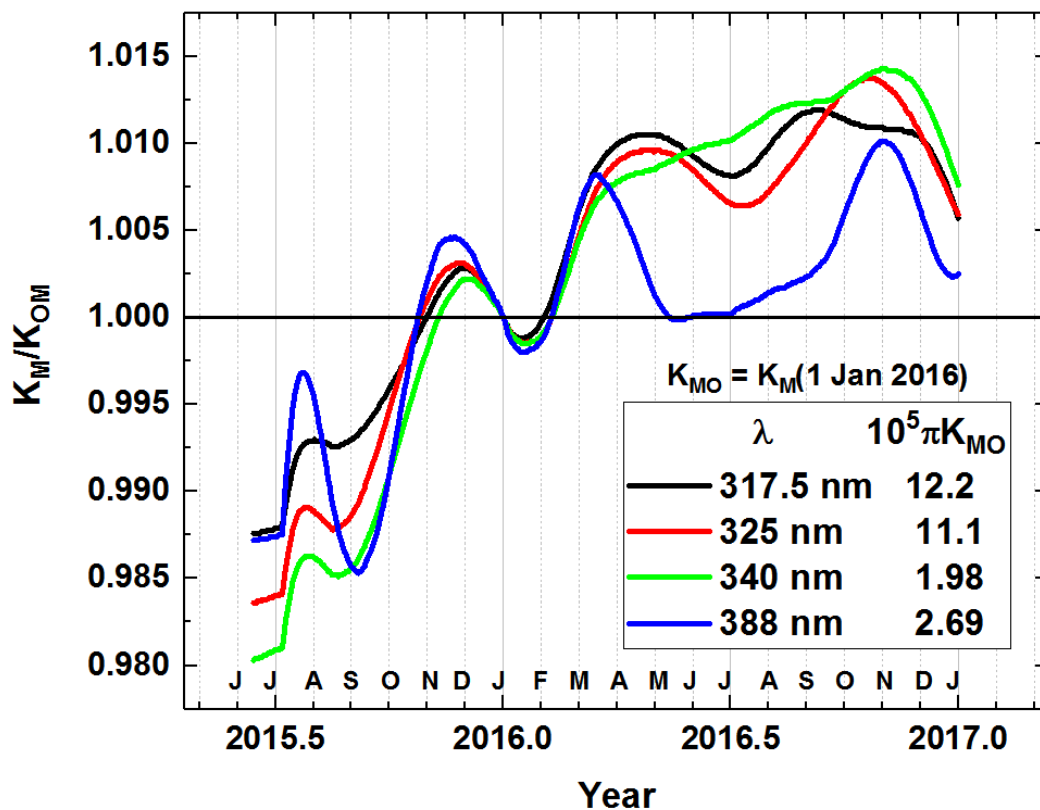
699 **Figures**

700



**f01**

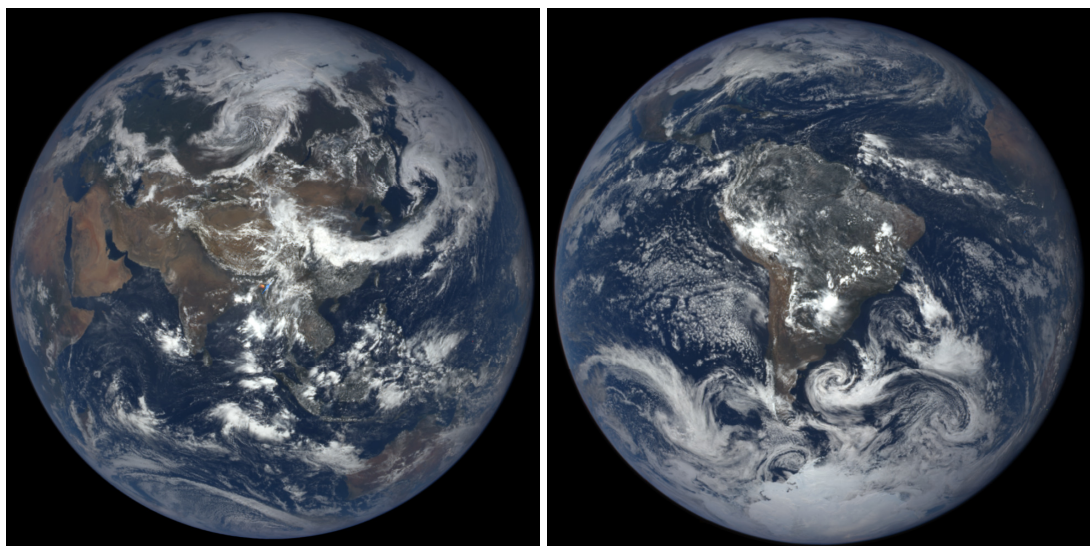
701



f02

702

703



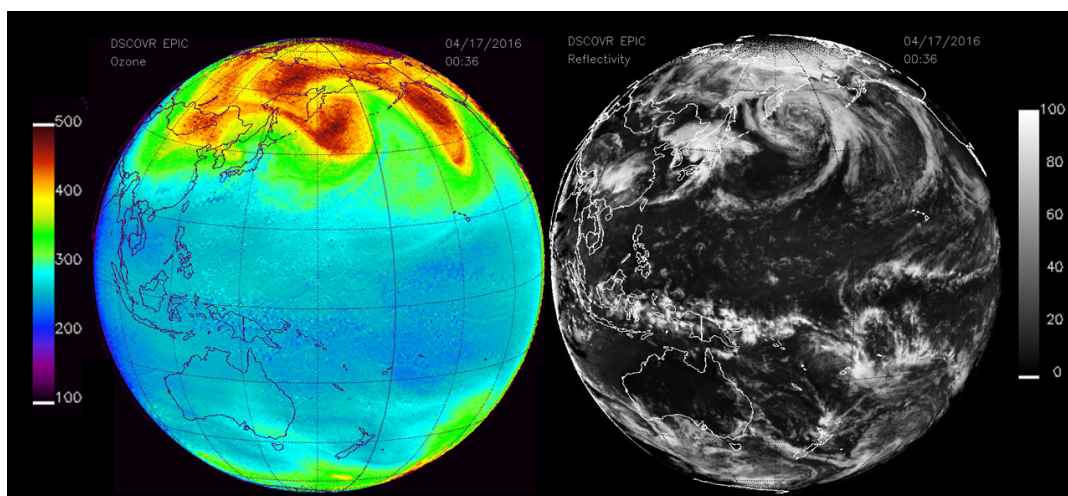
**f03**

704

705



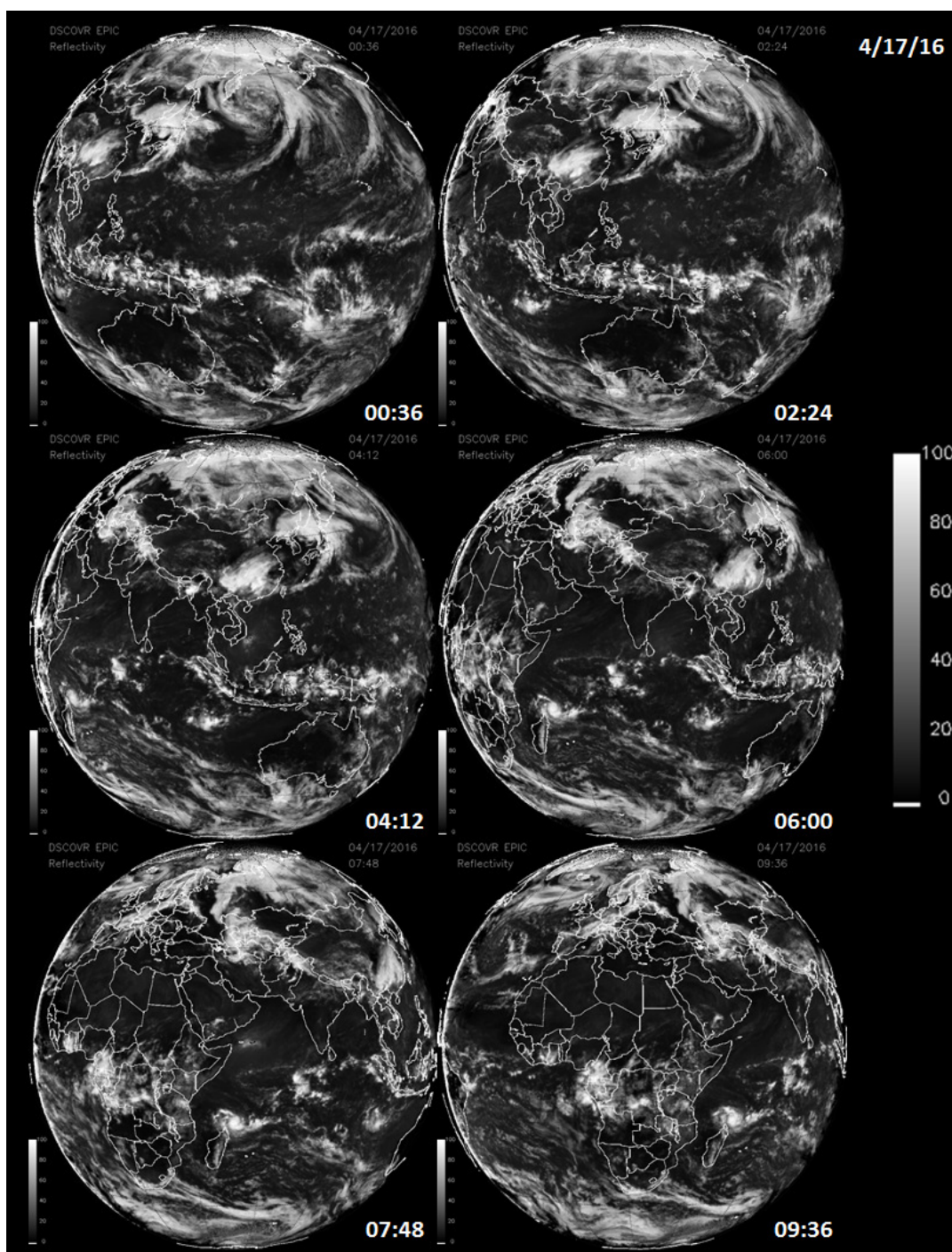
706



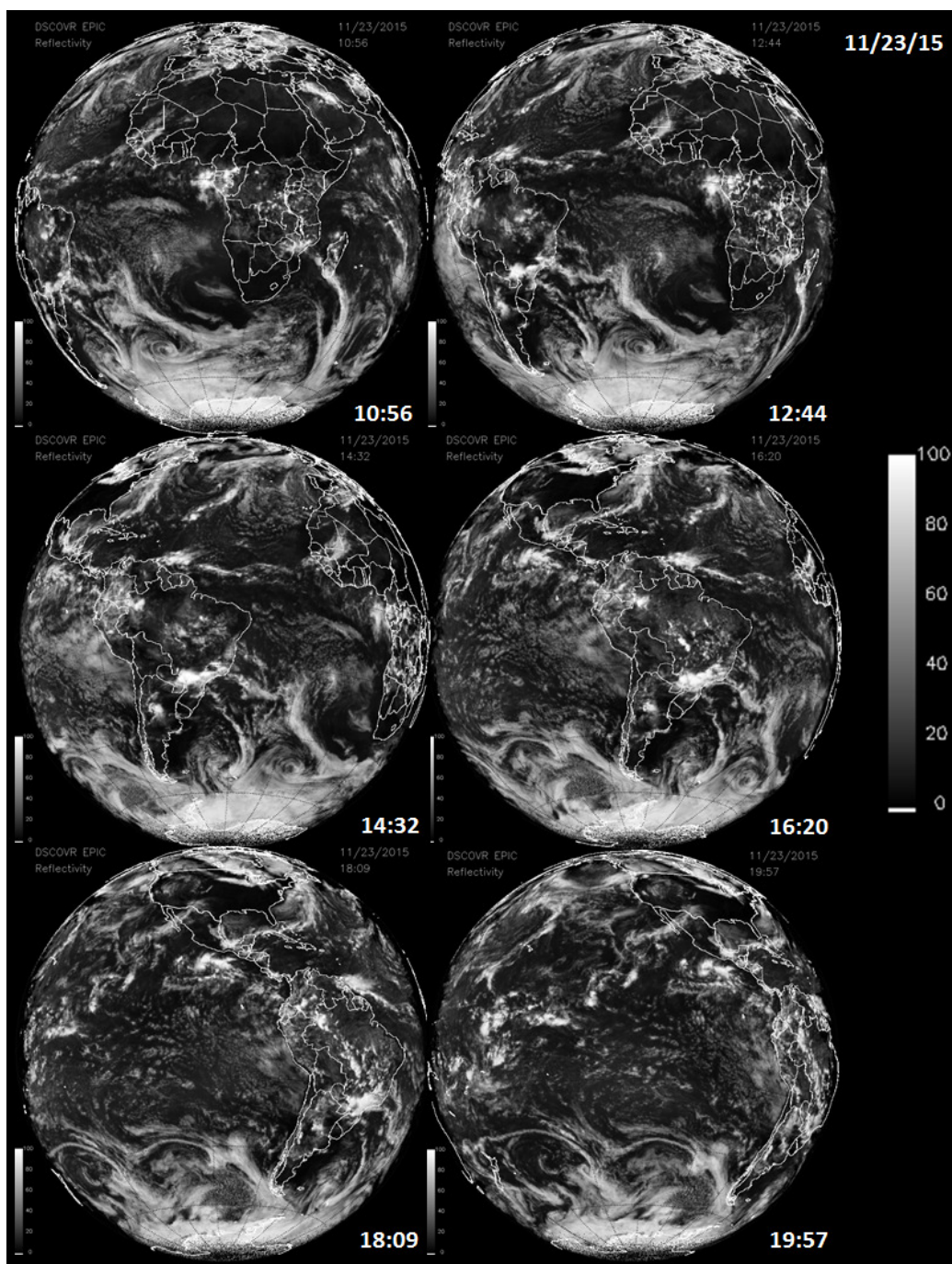
**f04**

707

708



f05

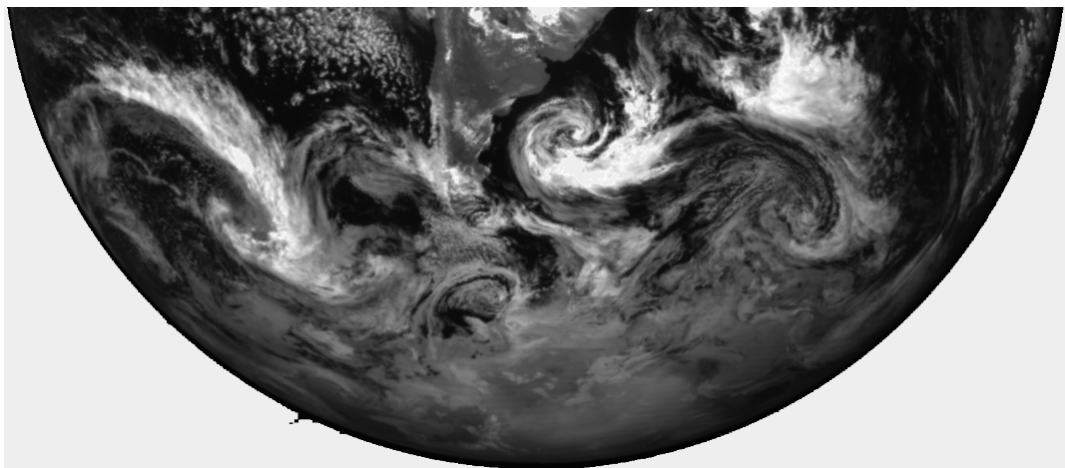


f06



709

710



**f07**

711

712

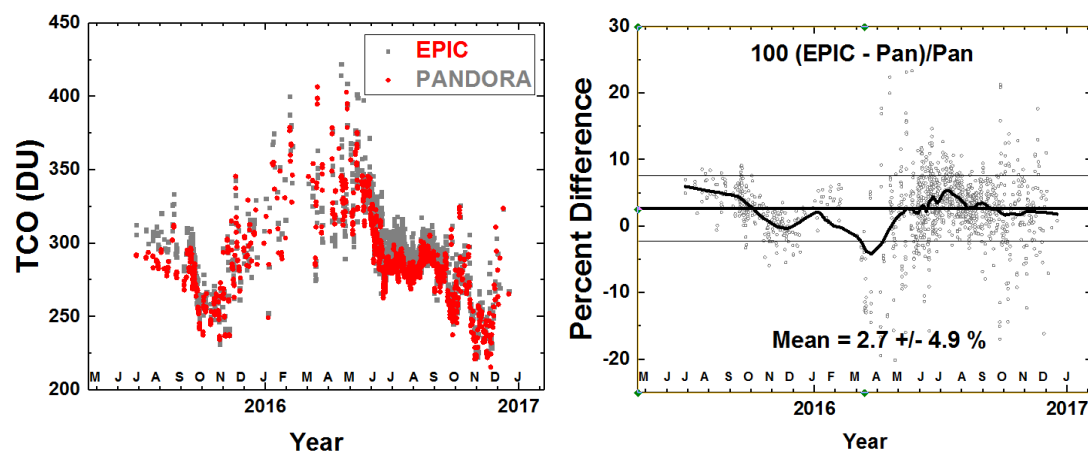




713

714

715

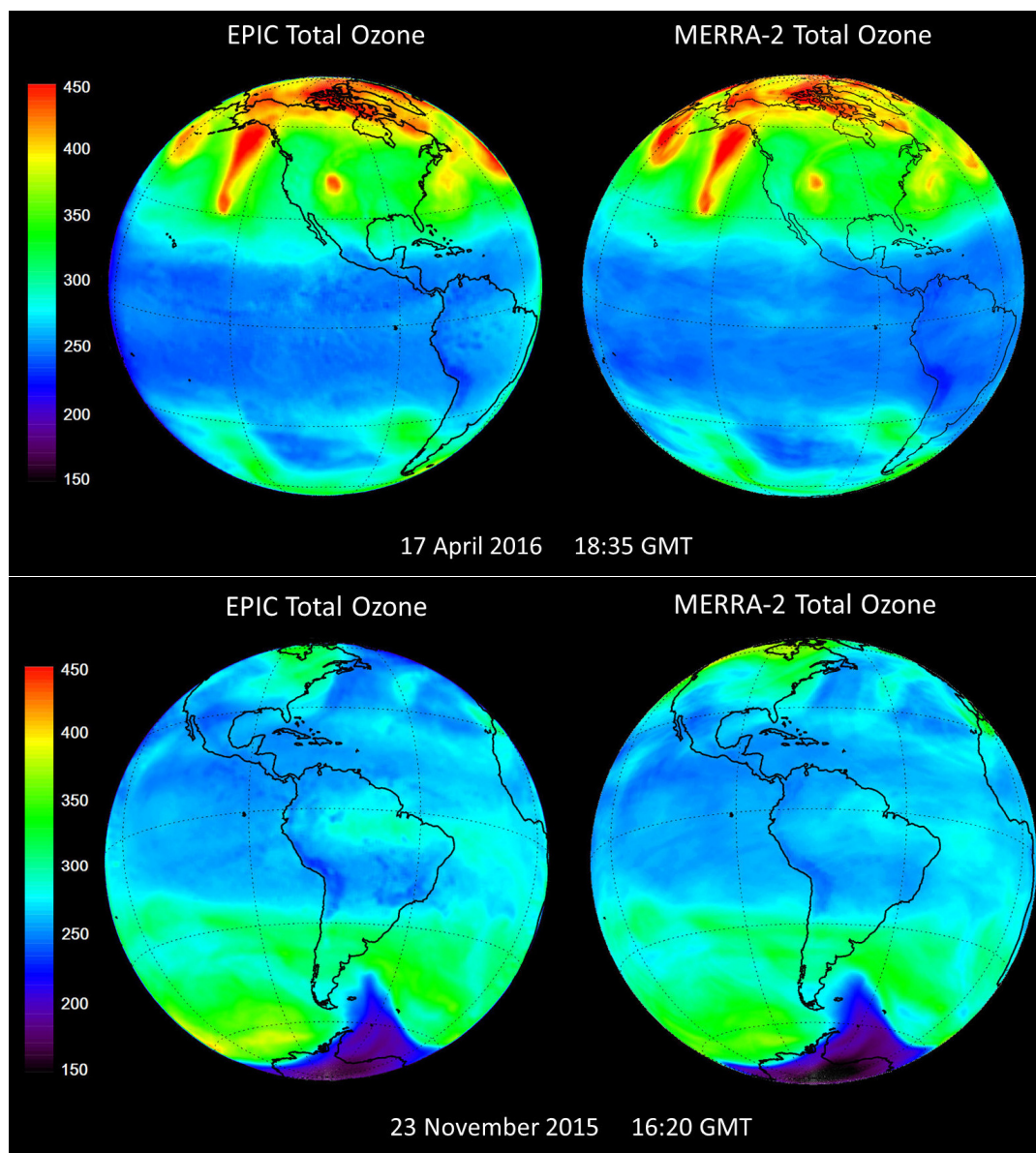


f08

716

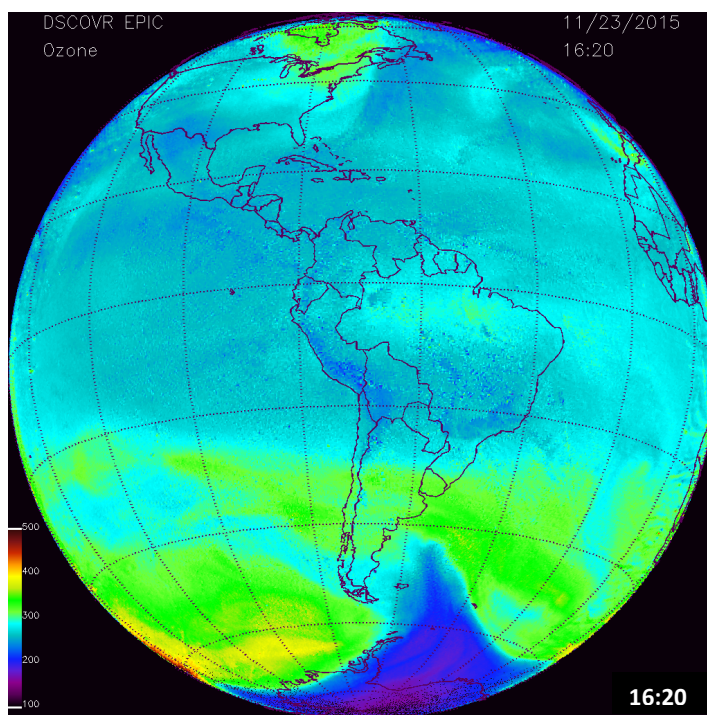


717



f09

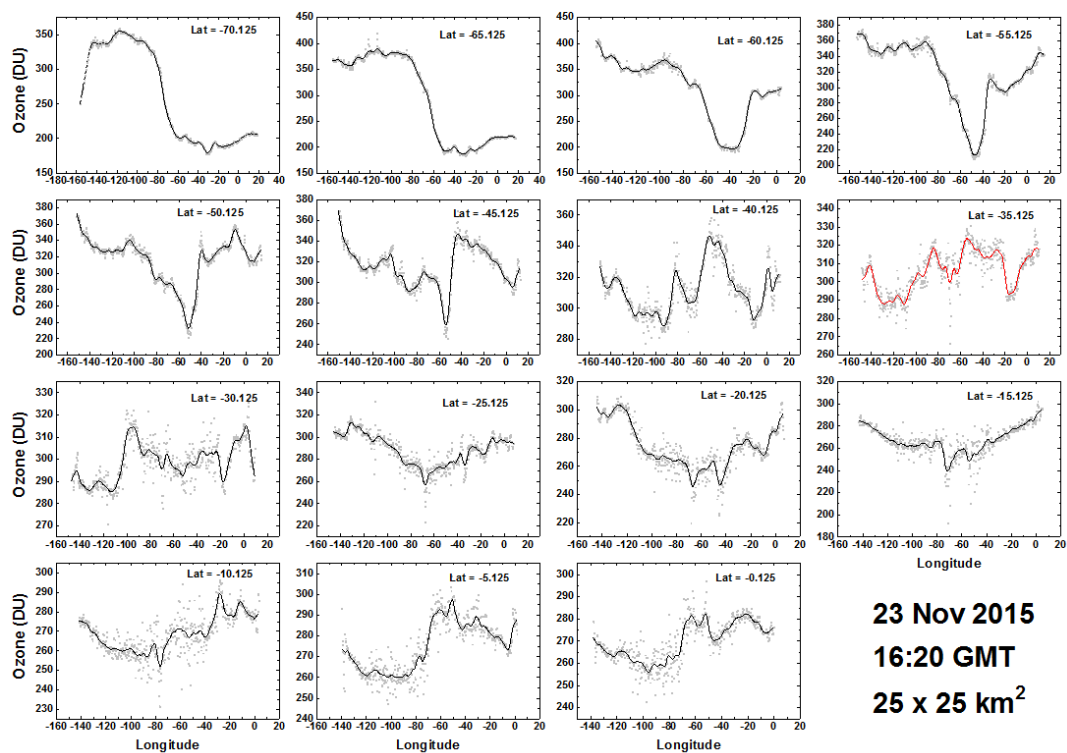
718



**f10**

719

720



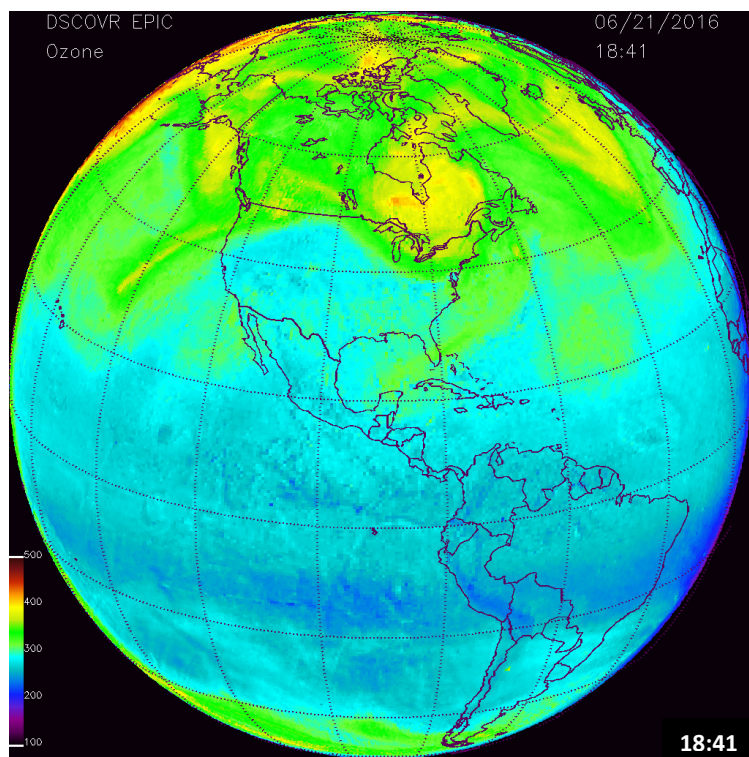
f11

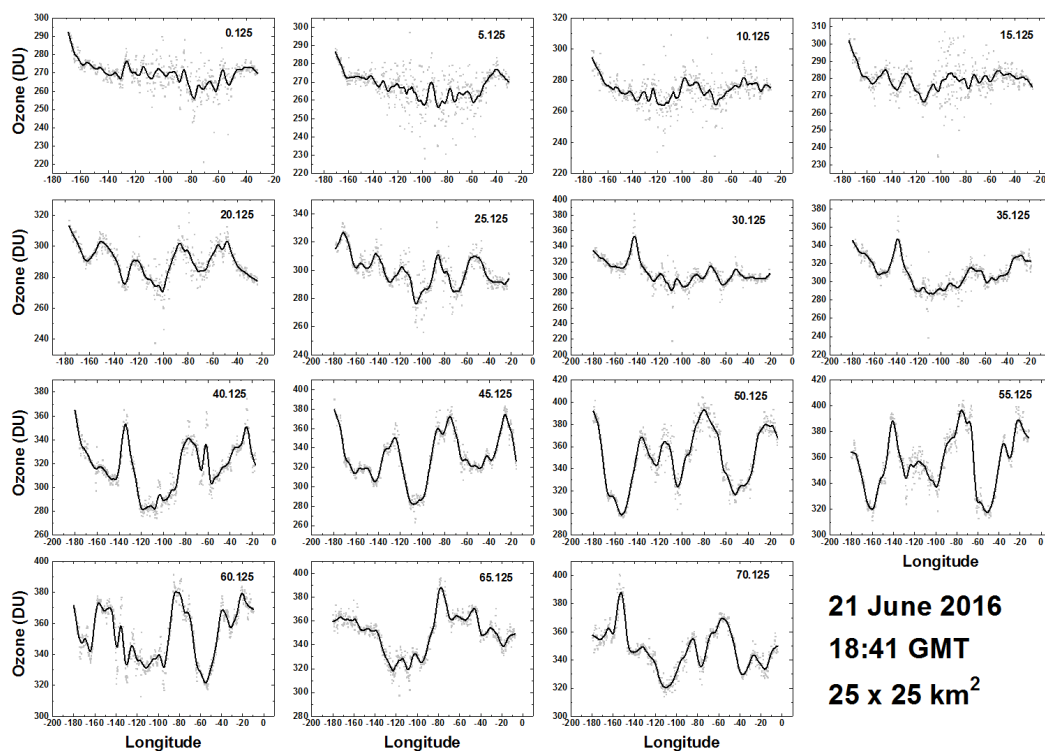
721

722



723  
724  
725  
726  
727  
728  
729  
730  
731  
732  
733  
734  
735  
736  
737  
738



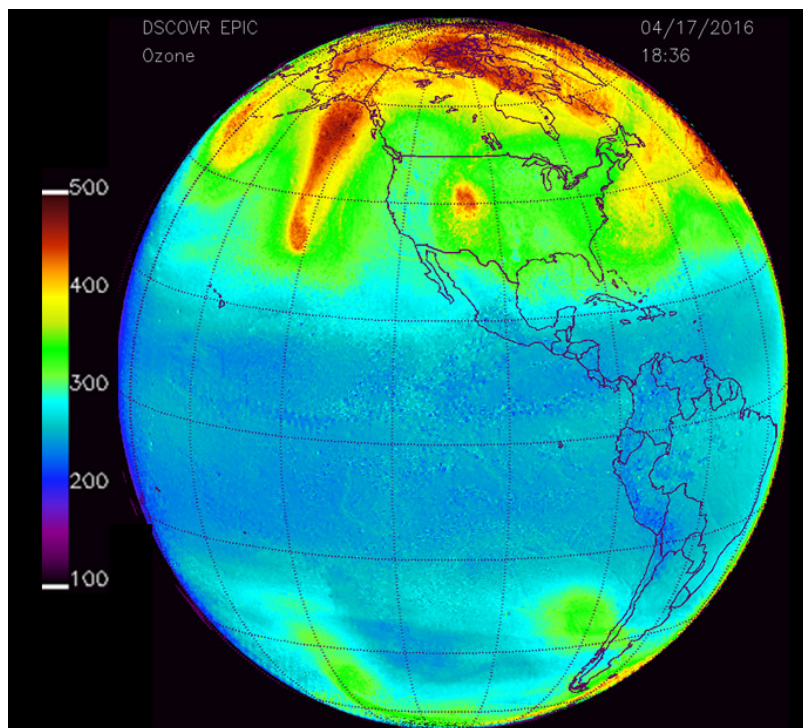


f13

739



740  
741  
742  
743  
744  
745  
746  
747  
748  
749

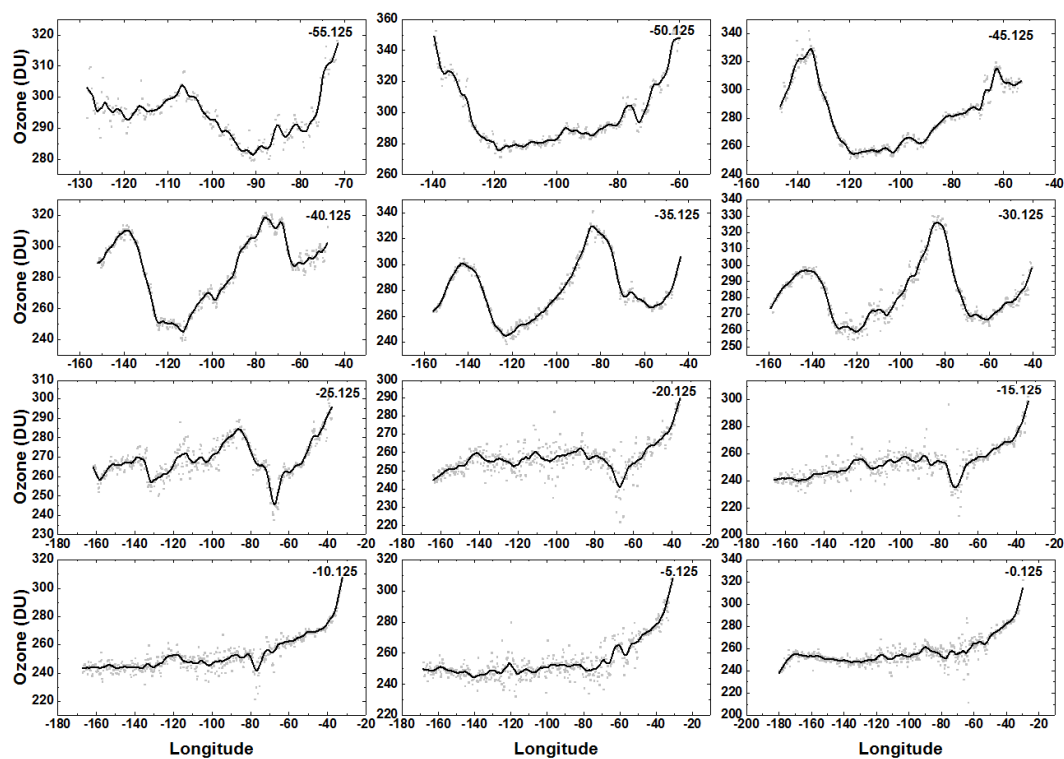


**f14**



750

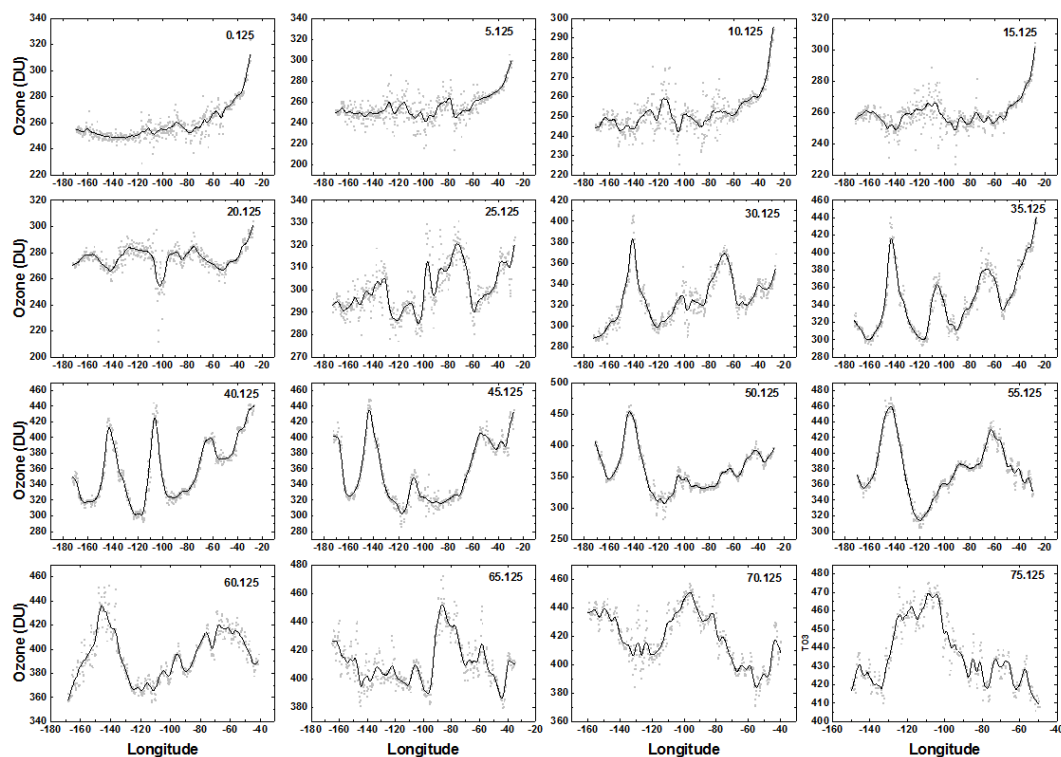
751



**f15**

752





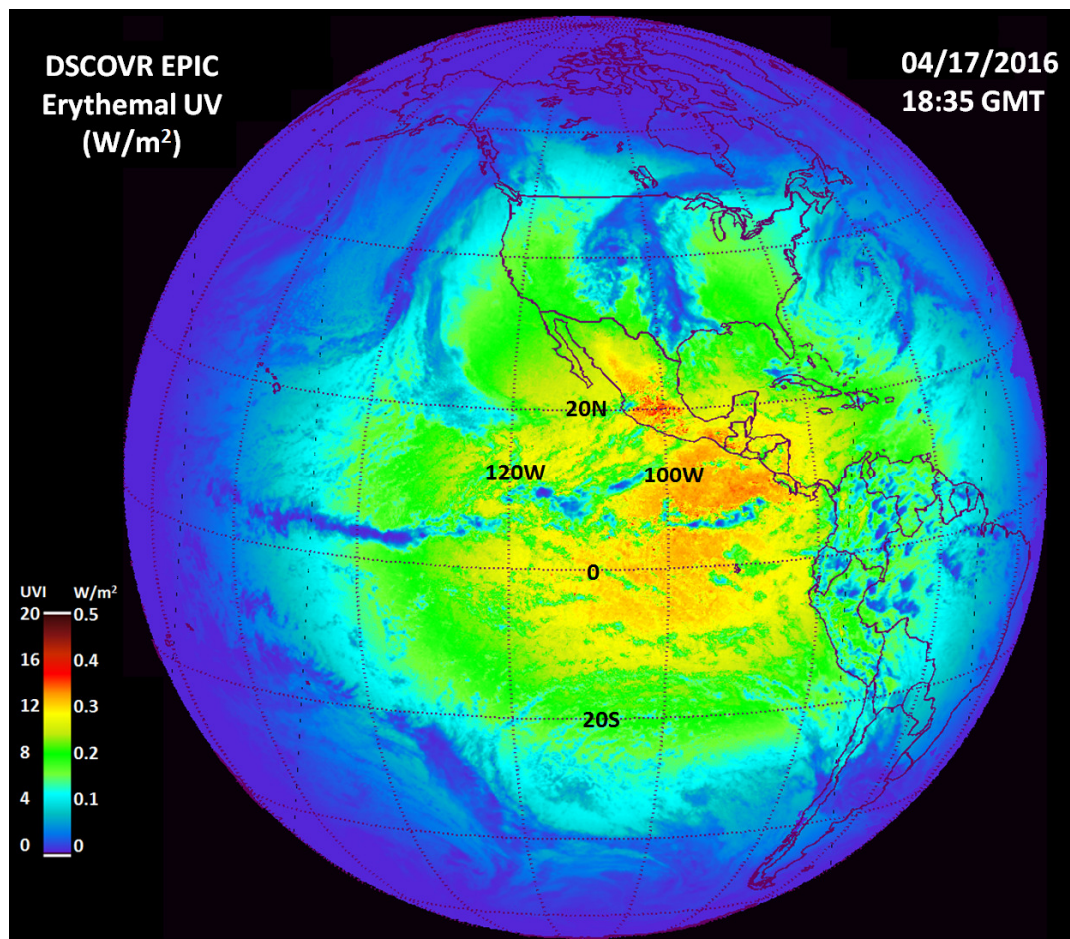
f16

753



754

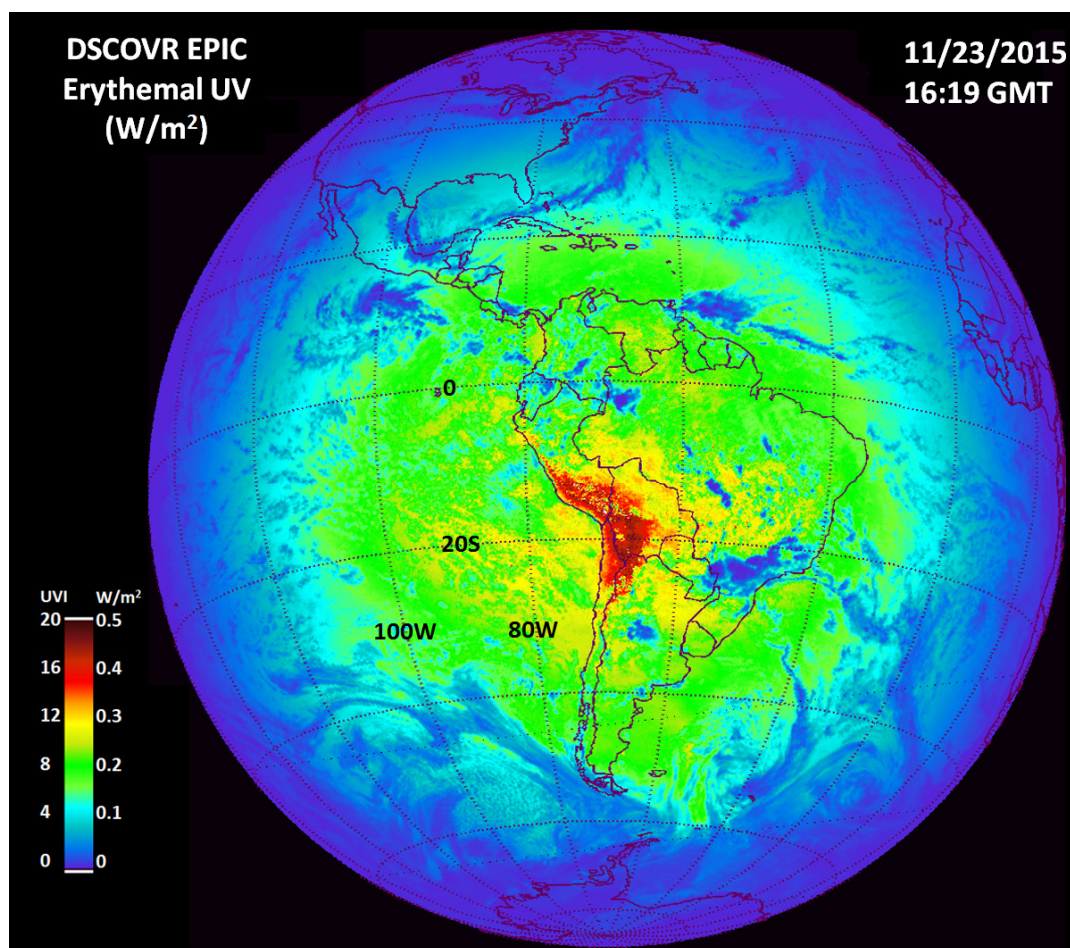
755



**f17**

756

757



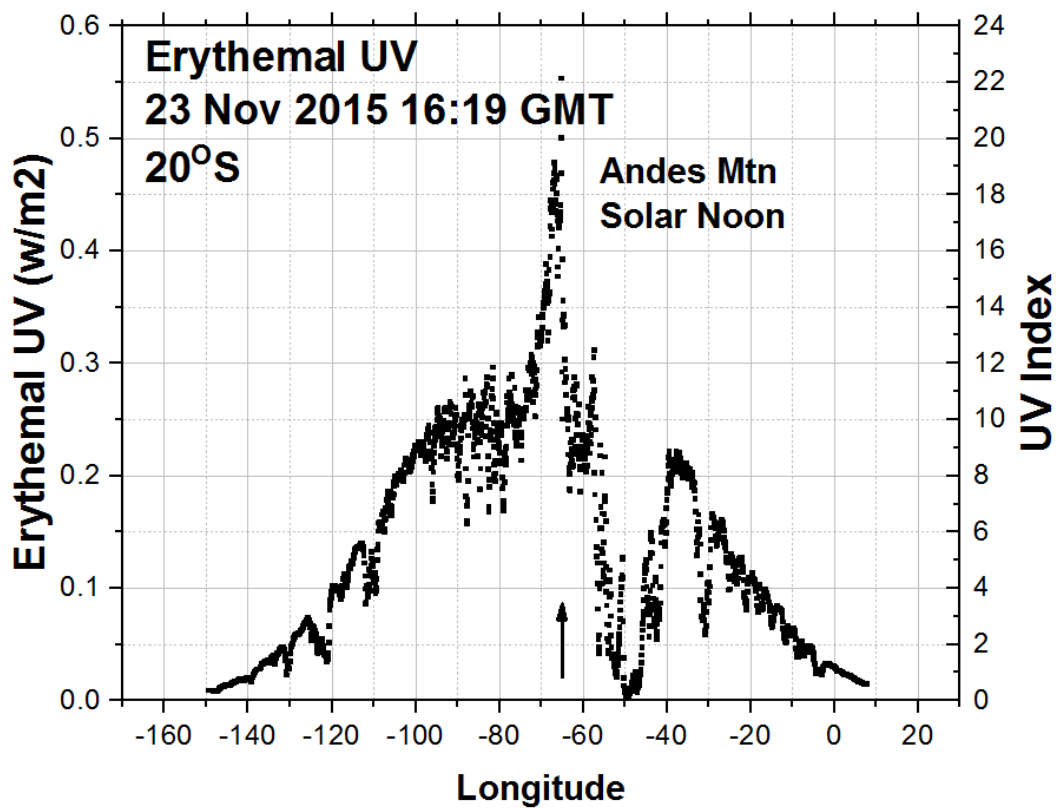
**f18**

758

759



760

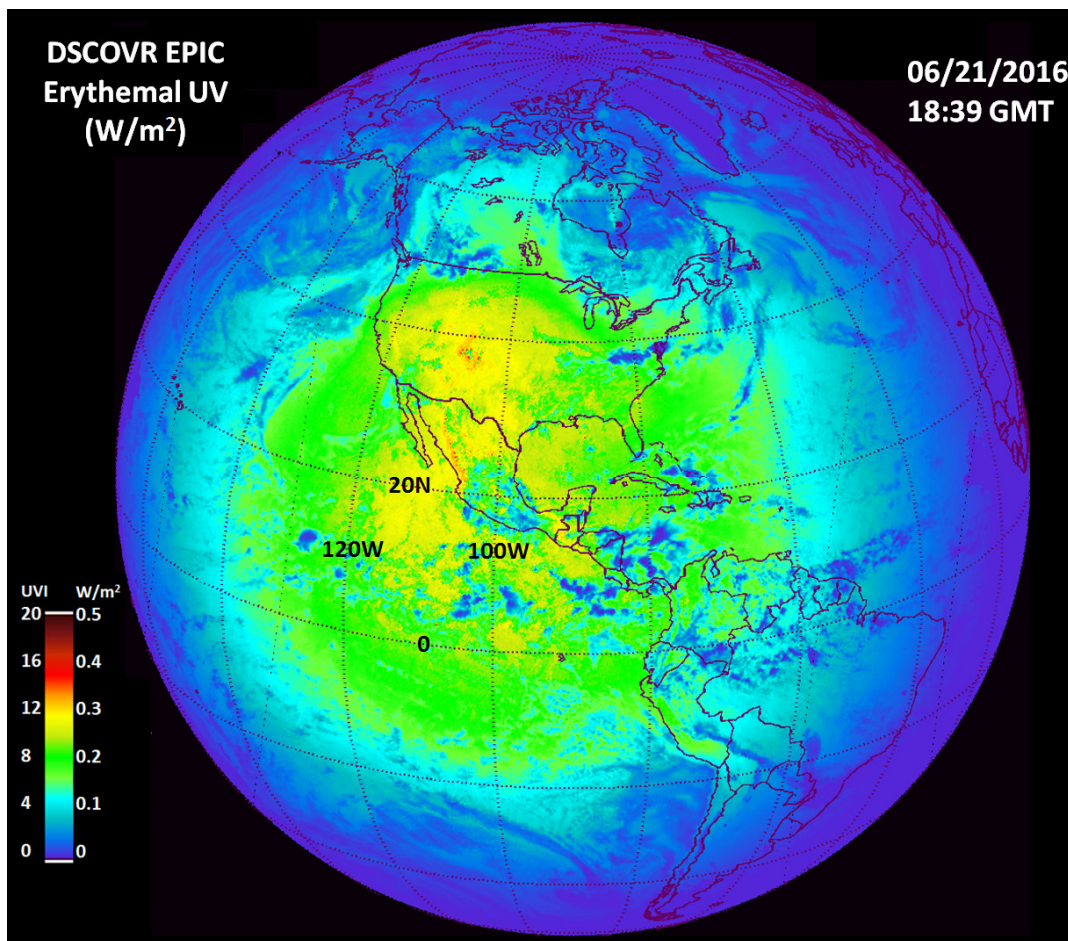


f19



761

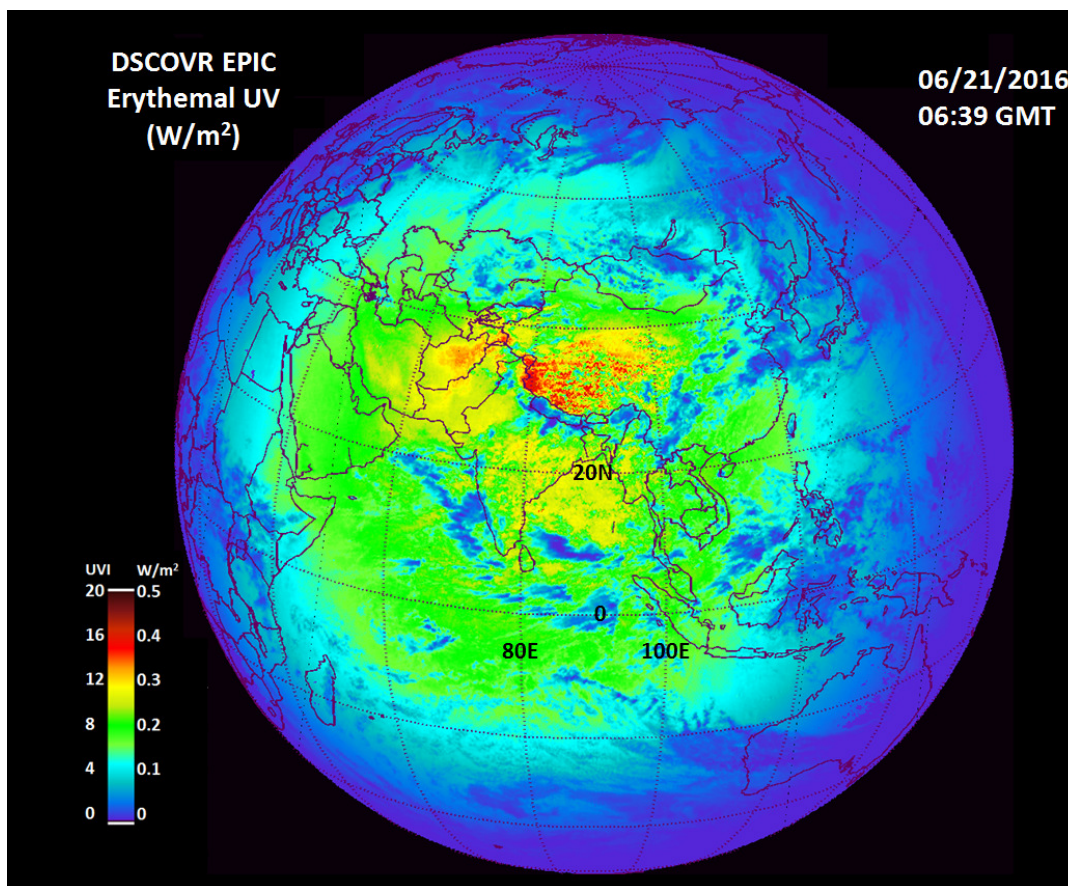
762



**f20**

763

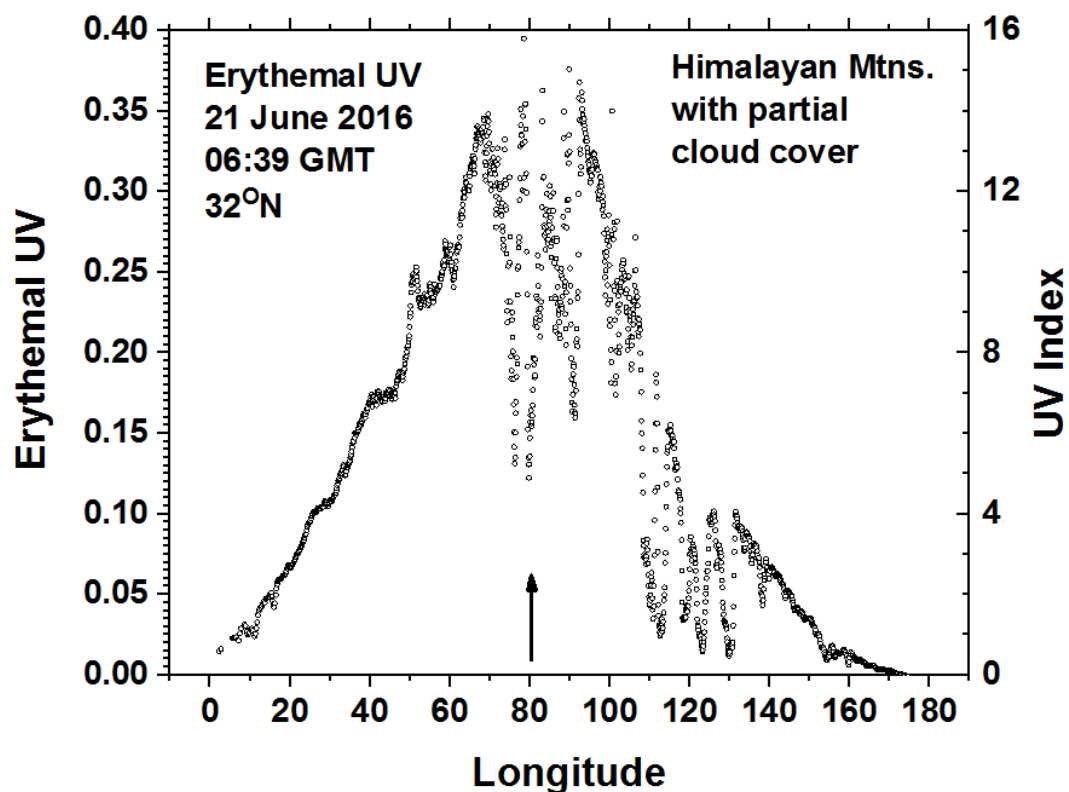
764



**f21**

765

766



f22

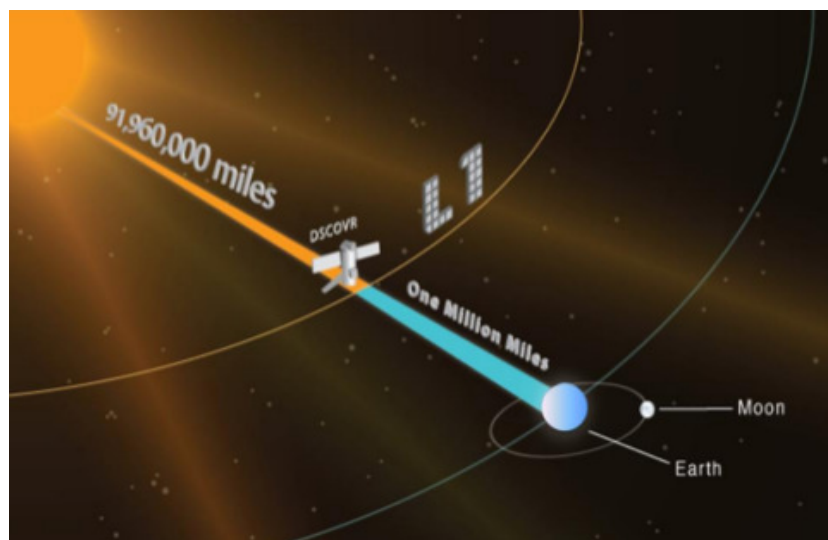
767

768

769

770

771



**fA1**

772